Monthly Notices of the ROYAL ASTRONOMICAL SOCIETY

MNRAS **535,** 3363–3382 (2024) https://doi.org/10.1093/mnras/stae2506
Advance Access publication 2024 November 8

SPIRou observations of the young planet-hosting star PDS 70

J.-F. Donati [1]★ P.I. Cristofari [2] S.H.P. Alencar,[3] Á. Kóspál,[4,5] J. Bouvier,[6] C. Moutou,[1] A. Carmona,[6] J. Gregorio-Hetem,[7] F. Ménard [8] E. Artigau,[9] R. Doyon,[9] M. Takami,[10] H. Shang [10] J. Dias do Nascimento [11] F. Ménard,[6] E. Gaidos [12] and the SPIRou science team

[1]*CNRS, IRAP, Université de Toulouse, 14 avenue Belin, F-31400 Toulouse, France*
[2]*Center for Astrophysics, Harvard & Smithsonian, 60 Garden street, Cambridge, MA 02138, USA*
[3]*Departamento de Física – ICEx – UFMG, Av. Antônio Carlos, 6627, 30270-901 Belo Horizonte, MG, Brazil*
[4]*Konkoly Observatory, HUN-REN Research Centre for Astronomy and Earth Sciences, Konkoly-Thege Miklós út 15-17, 1121 Budapest, Hungary*
[5]*Institute of Physics and Astronomy, ELTE Eötvös Loránd University, Pázmány Péter sétány 1/A, 1117 Budapest, Hungary*
[6]*CNRS, IPAG, Université Grenoble Alpes, F-38000 Grenoble, France*
[7]*IAG, Universidade de São Paulo, Rua do Matão 1226, SP-05508-090 São Paulo, Brazil*
[8]*European Southern Observatory, Karl-Schwarzschild-Strasse 2, D-85748 Garching bei München, Germany*
[9]*Département de Physique, IREX, Université de Montréal, Montréal, QC H3C 3J7, Canada*
[10]*Institute of Astronomy and Astrophysics, Academia Sinica, Roosevelt Rd, Taipei 10617, Taiwan*
[11]*Departamento de Física, UFRN, CP 1641, 59072-970, Natal, RN, Brazil*
[12]*Department of Earth Sciences, University of Hawaii at Manoa, 1680 East-West Rd, Honolulu, HI 96822, USA*

Accepted 2024 November 1. Received 2024 October 24; in original form 2024 August 24

ABSTRACT

This paper presents near-infrared spectropolarimetric and velocimetric observations of the young planet-hosting T Tauri star PDS 70, collected with SPIRou at the 3.6-m Canada–France–Hawaii Telescope from 2020 to 2024. Clear Zeeman signatures from magnetic fields at the surface of PDS 70 are detected in our data set of 40 circularly polarized spectra. Longitudinal fields inferred from Zeeman signatures, ranging from −116 to 176 G, are modulated on a time-scale of 3.008 ± 0.006 d, confirming that this is the rotation period of PDS 70. Applying Zeeman–Doppler imaging to subsets of unpolarized and circularly polarized line profiles, we show that PDS 70 hosts low-contrast brightness spots and a large-scale magnetic field in its photosphere, featuring in particular a dipole component of strength 200–420 G that evolves on a time-scale of months. From the broadening of spectral lines, we also infer that PDS 70 hosts a small-scale field of 2.51 ± 0.12 kG. Radial velocities derived from unpolarized line profiles are rotationally modulated as well, and exhibit additional longer term chromatic variability, most likely attributable to magnetic activity rather than to a close-in giant planet (with a 3σ upper limit on its minimum mass of $\simeq$4 $M_{\downarrow}$ at a distance of $\simeq$0.2 au). We finally confirm that accretion occurs at the surface of PDS 70, generating modulated redshifted absorption in the 1083.3-nm He I triplet, and show that the large-scale magnetic field, often strong enough to disrupt the inner accretion disc up to the corotation radius, weakens as the star gets fainter and redder (as in 2022), suggesting that dust from the disc more easily penetrates the stellar magnetosphere in such phases.

Key words: techniques: polarimetric – stars: formation – stars: imaging – stars: individual: PDS 70 – stars: magnetic fields – planetary systems.

1 INTRODUCTION

Over the last few decades, ground-based and space-borne observations have revealed a wealth of information on how low-mass stars and their planets build up from giant molecular clouds under the combined effect of turbulence, gravitation, and magnetic fields, first developing filamentary structures within which local overdensities, called dense cores, end up collapsing under their own weight (e.g. André et al. 2014). In this collapse, a rotating disc of gas and dust forms around the central mass, which progressively becomes a growing protostar through intense accretion from the disc, then a pre-main-sequence (PMS) star (also called T Tauri star / TTS) at an age of a few Myr, once accretion weakens and the newborn star gets warm enough to clear out its surrounding dust envelope through radiation and outflows (e.g. Tsukamoto et al. 2023; Cabrit 2024; Kuffmeier 2024). Planets form more or less at the same time, with gas and dust particles within the disc colliding together and growing into pebbles, then planetesimals, before becoming actual protoplanets (e.g. Drążkowska et al. 2023). Giant planets presumably form in the outer, cooler regions of the protoplanetary disc, beyond the snow line, where they can accumulate large amounts of hydrogen and helium, and may start migrating inward within the disc before it dissipates at an age of 3–10 Myr, to eventually become close-in giant planets, shaping at the same time the architecture of planetary

★ E-mail: jean-francois.donati@irap.omp.eu

systems (e.g. Mordasini et al. 2012; Chambers 2018; Lau et al. 2024). Magnetic fields play a key role at virtually all stages in this process, by affecting the dynamics and impacting fragmentation within the disc, by altering the way disc material is accreted onto the star and planets, and by influencing how planets form and migrate within the disc (e.g. Pudritz & Ray 2019).

Whereas observations of TTSs with multiple techniques operating at various wavelengths have allowed us to investigate in detail the key physical mechanisms at work in star formation, including magnetospheric accretion and ejection phenomena taking place between the star and the accretion disc (Hartmann, Herczeg & Calvet 2016; Hussain 2018; Bouvier 2022), much less is known from actual data about forming planets at an age of a few Myr, with only a few young planets detected so far around low-mass stars either directly through imaging (e.g. Xie et al. 2020; Langlois et al. 2021), or indirectly through transit photometry or velocimetry (e.g. David et al. 2019; Mann et al. 2022). Whereas the first approach is technically tricky given the combination of high-angular resolution and high-contrast performance that it mandatorily requires, the second one is just as complex, the size of the photometric or velocimetric signals being vastly smaller, even for close-in giant planets, than the huge spectral variability that TTSs exhibit as a result of accretion and magnetic activity. This is why only a handful of planets around stars younger than 20 Myr have reliably been identified by such techniques so far.

Initially identified as a PMS star (Gregorio-Hetem et al. 1992; Gregorio-Hetem & Hetem 2002) through its spectral features (in particular Hα emission and 670.7-nm Li absorption) and the infrared excess indicating the presence of an extended accretion disc, PDS 70 is a very interesting target in this respect, as outlined more extensively in Section 2. Featuring a highly structured accretion disc with a large central cavity hosting two massive protoplanets (Keppler et al. 2018; Haffert et al. 2019), PDS 70 is the only TTS so far with multiple directly imaged forming planets and thereby a key object for studying the late phases of protoplanetary disc evolution and planet formation. At an age of about $\simeq$5 Myr, both the star and the two distant giant planets (possibly even younger than the star) are still in the process of accreting material from the surrounding disc, offering us a glimpse into stages of planetary development that are only observable in young systems and hard to infer from data on older systems. PDS 70 thereby provides us with the opportunity of bridging the gap between theoretical models and observations of planet formation.

Our paper is structured as follows. After a short revisit of the main characteristics of PDS 70 in Section 2, we detail our new near-infrared (nIR) SPIRou observations in Section 3, outline the spectropolarimetric results obtained for this star (in Section 4) and the tomographic modelling inferred with Zeeman–Doppler Imaging (ZDI, see Section 5). We also present the velocimetric study based on our SPIRou data (in Section 6) as well as a short analysis of the few nIR emission lines of PDS 70 (in Section 7). We conclude with a final summary of our results and a short discussion on what they tell us about star and planet formation (in Section 8).

2 THE T TAURI STAR PDS 70

PDS 70 (V1032 Cen, CD-40 8434, IRAS 14050−4109) is a TTS located at a distance of 112.4 ± 0.3 pc from the Sun (Gaia Collaboration 2023) in the Sco-Cen association. PDS 70 was first identified as a weak-line TTS (Gregorio-Hetem et al. 1992; Gregorio-Hetem & Hetem 2002), i.e. a TTS that experiences no accretion at the surface and thereby exhibits only weak emission lines. The highly structured accretion disc of PDS 70 indeed features a large central dust-depleted cavity (Hashimoto et al. 2012), within which two massive protoplanets were detected through direct imaging (at radii of 21 and 35 au), and shown to be accreting from a circumplanetary disc (Keppler et al. 2018; Haffert et al. 2019; Isella et al. 2019; Thanathibodee et al. 2019; Benisty et al. 2021; Blakely et al. 2024). PDS 70 itself was finally also proven to be accreting from an inner disc (of radius $\simeq$10 au), albeit at very low accretion rates (Haffert et al. 2019; Thanathibodee et al. 2020).

The photospheric temperature of PDS 70 was initially measured at $T_{\rm eff} = 4400 \pm 100$ K from fitting the spectral energy distribution (Gregorio-Hetem & Hetem 2002), then later revised to better match its $B - V = 1.24$ colour index, in agreement with a cooler temperature of $T_{\rm eff} = 4020$ K (with $A_{\rm V} \simeq 0$, Pecaut & Mamajek 2013) or 4140 K (with $A_{\rm V} \simeq 0.2$). The putatively most accurate set of photospheric parameters were derived from the latest *Gaia* data (DR3), yielding $T_{\rm eff} = 4140 \pm 10$ K and $\log g = 4.15 \pm 0.01$ (Gaia Collaboration 2023). Given the minimum V magnitude (unspotted brightness) of PDS 70, equal to $V = 12.05$ according to the ASAS-SN V-band photometry (Kochanek et al. 2017, see top panel of Fig. A1 in Appendix A), the quoted distance and photospheric temperature (implying a bolometric correction of −0.95, Pecaut & Mamajek 2013), we infer for this star a logarithmic luminosity with respect to the Sun equal to $\log(L_\star/{\rm L}_\odot) = -0.36 \pm 0.04$ and thereby a radius of $R_\star = 1.29 \pm 0.06{\rm R}_\odot$. Besides, a precise mass estimate of $M_\star = 0.875 \pm 0.030{\rm M}_\odot$ was derived for PDS 70 from the disc gas kinematics observed with ALMA (Keppler et al. 2019). Coupled to the $\log g$ estimate from *Gaia*, we can infer an independent radius estimate for PDS 70, equal to $R_\star = 1.31 \pm 0.06{\rm R}_\odot$ and in good agreement with the previous one. In the following, we take the average between both estimates and thus assume that PDS 70 has a radius of $R_\star = 1.30 \pm 0.06{\rm R}_\odot$, implying at the same time $\log(L_\star/{\rm L}_\odot) = -0.35 \pm 0.04$.

Comparing to the evolutionary models of Baraffe et al. (2015), we infer from $T_{\rm eff}$ and $\log g$ a stellar mass of $M_\star = 0.86 \pm 0.01{\rm M}_\odot$, very close to the dynamical mass of Keppler et al. (2019), and an age of 5.8 ± 0.3 Myr, consistent with other literature estimates. We note that in the particular case of PDS 70, the mass derived from the evolutionary models of Baraffe et al. (2015) is not overestimated by $\simeq$30 per cent, as opposed to what was inferred for this mass range from several other PMS stars for which dynamical masses were also available (Braun et al. 2021). At this age, PDS 70 is most likely no longer fully convective, with about 20 per cent of the central mass forming a radiative core (according to Baraffe et al. 2015).

The rotation period we derive for PDS 70 from spectropolarimetry, equal to $P_{\rm rot} = 3.008 \pm 0.006$ d (see Section 4), is consistent with the previously published estimate (Thanathibodee et al. 2020) and with that inferred from the ASAS-SN V- and g-band light curves (3.010 ± 0.010 d, see Section 4 and Fig. A2). Once coupled to our measurement of the line-of-sight projected equatorial rotation velocity of PDS 70 $v \sin i = 19.0 \pm 0.5$ km s^{-1} derived from brightness and magnetic mapping with ZDI (see Section 5), it yields $R_\star \sin i = 1.13 \pm 0.03{\rm R}_\odot$, thus implying an inclination of the rotation axis of PDS 70 to the line of sight of $i = 60^\circ \pm 6^\circ$. This is slightly larger than (though still roughly consistent with) the inclination of the normal of the outer disc to the line of sight (equal to $i_{\rm disc} = 51.7^\circ$, Keppler et al. 2019), suggesting that any potential misalignment between the equatorial plane of PDS 70 and its surrounding disc should be small. The corotation radius, at which the Keplerian angular rotation rate equals the angular rotation rate at the surface of the star, is equal to $r_{\rm cor} = 0.039 \pm 0.001$ au ($6.5 \pm 0.3 R_\star$).

Table 1. Parameters of PDS 70 used in or derived from our study.

Distance (pc)	112.4 ± 0.3	Gaia Collaboration (2023)
$T_{\rm eff}$ (K)	4140 ± 10	Gaia Collaboration (2023)
$\log g$ (dex)	4.15 ± 0.01	Gaia Collaboration (2023)
$M_\star$ ($M_\odot$)	0.875 ± 0.030	Keppler et al. (2019)
$R_\star$ ($R_\odot$)	1.30 ± 0.06	
$\log(L_\star/L_\odot)$	-0.35 ± 0.04	
Age (Myr)	5.8 ± 0.3	Baraffe et al. (2015)
$P_{\rm rot}$ (d)	3.010	Period used to phase data
$P_{\rm rot}$ (d)	3.008 ± 0.006	From B_ℓ data
$P_{\rm rot}$ (d)	3.010 ± 0.009	From ASAS-SN V and g data
$v \sin i$ (km s^{-1})	19.0 ± 0.5	From ZDI modelling
$R_\star \sin i$ ($R_\odot$)	1.13 ± 0.03	From $R_\star$ and $v \sin i$
i (°)	60 ± 6	From $R_\star$ and $R_\star \sin i$
$i_{\rm disc}$ (°)	51.7 ± 0.1	Keppler et al. (2019)
$<B>$ (kG)	2.51 ± 0.12	On median spectrum
$r_{\rm cor}$ (au)	0.039 ± 0.001	From $M_\star$ and $P_{\rm rot}$
$r_{\rm cor}$ ($R_\star$)	6.5 ± 0.3	From $r_{\rm cor}$ (au) and $R_\star$
$\log \dot{M}$ ($M_\odot$ yr^{-1})	-10.3 to -9.7	Thanathibodee et al. (2020)

The logarithmic mass accretion rate $\log \dot{M}$ reported to take place at the surface of PDS 70 is low, ranging from -10.3 to -9.7 (in $M_\odot$ yr^{-1}, with an uncertainty of about 0.3, Haffert et al. 2019; Thanathibodee et al. 2020; Skinner & Audard 2022; Campbell-White et al. 2023; Gaidos et al. 2024). Although weak, accretion can significantly distort the light curve, with rotational modulation getting weaker (see e.g. the stacked periodogram of the ASAS-SN V- and g-band light curves in Fig. A2), sometimes to the point of vanishing, as in the sector 38 and 65 *TESS* light curves (Gaidos et al. 2024). Using the wind-tracing 630-nm [O I] line, a magnetically driven disc wind was also detected in the inner disc of PDS 70, originating from a radius of 0.1–0.2 au (Campbell-White et al. 2023). We come back on these points in Section 7.

All stellar parameters used in or derived from this study are listed in Table 1.

3 SPIROU OBSERVATIONS

We observed PDS 70 in three different seasons with the SPIRou nIR spectropolarimeter/high-precision velocimeter (Donati et al. 2020) at the 3.6-m Canada-France-Hawaii Telescope (CFHT), within the SPIRou Legacy Survey (SLS) in 2020 May and June, and 2022 June, then within the SPICE Large Programme in 2024 March–May. SPIRou collects unpolarized and polarized stellar spectra, covering a wavelength interval of 0.95–2.50 μm at a resolving power of 70 000 in a single exposure. In this study, we focused on circularly polarized (Stokes V) and unpolarized (Stokes I) spectra only. Polarization observations usually consist of sequences of four subexposures, with each subexposure corresponding to a different azimuth of the Fresnel rhomb retarders of the SPIRou polarimetric unit. This procedure was shown to succeed in removing systematics in polarization spectra (to first order, see e.g. Donati et al. 1997). Each recorded sequence yields one Stokes I and one Stokes V spectrum, as well as one null polarization check (called N) used to diagnose potential instrumental or data reduction issues. In case of unstable weather conditions where only two subexposures can be recorded, one can still retrieve a pair of Stokes I and V spectra, but no N spectrum and a slightly worse compensation of systematics.

We recorded a total of 43 polarization sequences for PDS 70, 4 in 2020, 10 in 2022, and 29 in 2024, with a single sequence collected in most clear nights. As a result of poor weather leading to very low signal-to-noise ratios (SNRs), three spectra were discarded, one in the second season (on June 13) and two in the third one (on April 30 and May 28); weather issues also caused one sequence of the second season (on June 12) to include only two subexposures. Our final data set thus included 40 validated Stokes I and V spectra of PDS 70 over three seasons, with seasonal subsets respectively spanning intervals of 27 d (4 points), 10 d (9 points), and 71 d (27 points), and altogether covering a temporal window of 1480 d. The full log of our observations is provided in Table B1 in Appendix B.

All SPIRou spectra of PDS 70 were processed with LIBRE ESPRIT, the nominal reduction pipeline of ESPaDOnS at CFHT, optimized for spectropolarimetry and adapted for SPIRou (Donati et al. 2020). Subsequently, we applied least-squares deconvolution (LSD, Donati et al. 1997) to the reduced spectra, with a line mask computed with the VALD-3 database (Ryabchikova et al. 2015) for a set of atmospheric parameters ($T_{\rm eff} = 4000$ K and $\log g = 4.0$) matching those of PDS 70 (see Section 2). As in previous studies, we only selected atomic lines deeper than 10 per cent of the continuum level, for a total of $\simeq$1500 lines of average wavelength and Landé factor equal to 1750 nm and 1.2, respectively. The noise levels σ_V in the resulting Stokes V LSD profiles range from 1.9 to 4.8 (median 2.2, in units of $10^{-4} I_c$ where I_c denotes the continuum intensity). These Stokes I and V LSD profiles were mostly used to investigate the magnetic properties of PDS 70 (see Sections 4 and 5) as well as its velocimetric behaviour (see Section 6), and to estimate the spectral veiling (in the J and H bands mostly) reducing the depth of spectral lines as a result of accretion (see Section 7). We also constructed a second LSD mask, containing the $\simeq$300 CO lines of the CO bandhead only, known to be insensitive to magnetic fields, to help diagnose the impact of activity on radial velocities (RVs, see Section 6) and measure the veiling in the K band (see Section 7).

Phases and rotation cycles are derived assuming a rotation period of $P_{\rm rot} = 3.010$ d (see Table 1) and counting from an arbitrary starting BJD0 of 2458977.9 (i.e. prior to our first SPIRou observation).

4 SPECTROPOLARIMETRIC ANALYSIS

The inferred Stokes I and V LSD profiles of PDS 70 show clear Zeeman signatures within spectral lines. This is best evidenced by deriving the longitudinal field B_ℓ, i.e. the line-of-sight projected component of the vector field at the surface of the star averaged over the visible stellar hemisphere, associated with each pair of Stokes V and I LSD profiles following Donati et al. (1997). In practice, we achieve this by computing the first moment of the Stokes V profile and its error bar, which we normalize with the equivalent width (EW) of the Stokes I LSD profiles estimated through a standard Gaussian fit. Given the $v \sin i$ of PDS 70 (of 19.0 ± 0.5 km s^{-1}, see Section 5), the first moment of Stokes V LSD profiles were computed on a window of ± 34 km s^{-1} in the stellar rest frame in order not to miss some of the polarimetric information and yet minimize the impact of photon noise. We find that B_ℓ varies from -116 to 176 G (median 66 G) over our observing campaign with error bars ranging from 10 to 30 G (median 13 G), implying a reduced chi-square $\chi^2_{\rm r}$ (with respect to the $B_\ell = 0$ G level) equal to $\chi^2_{\rm r} = 47.9$ and thus a very clear magnetic detection. Processing the polarization check N in the same way yields $\chi^2_{\rm r} = 1.16$, consistent with no signal and indicating that our spectropolarimetric measurements are free of spurious pollution and that our formal error bars agree with the observed measurement dispersion.

To investigate rotational modulation of our B_ℓ data, allowing for temporal evolution of the modulation pattern, we proceeded as in

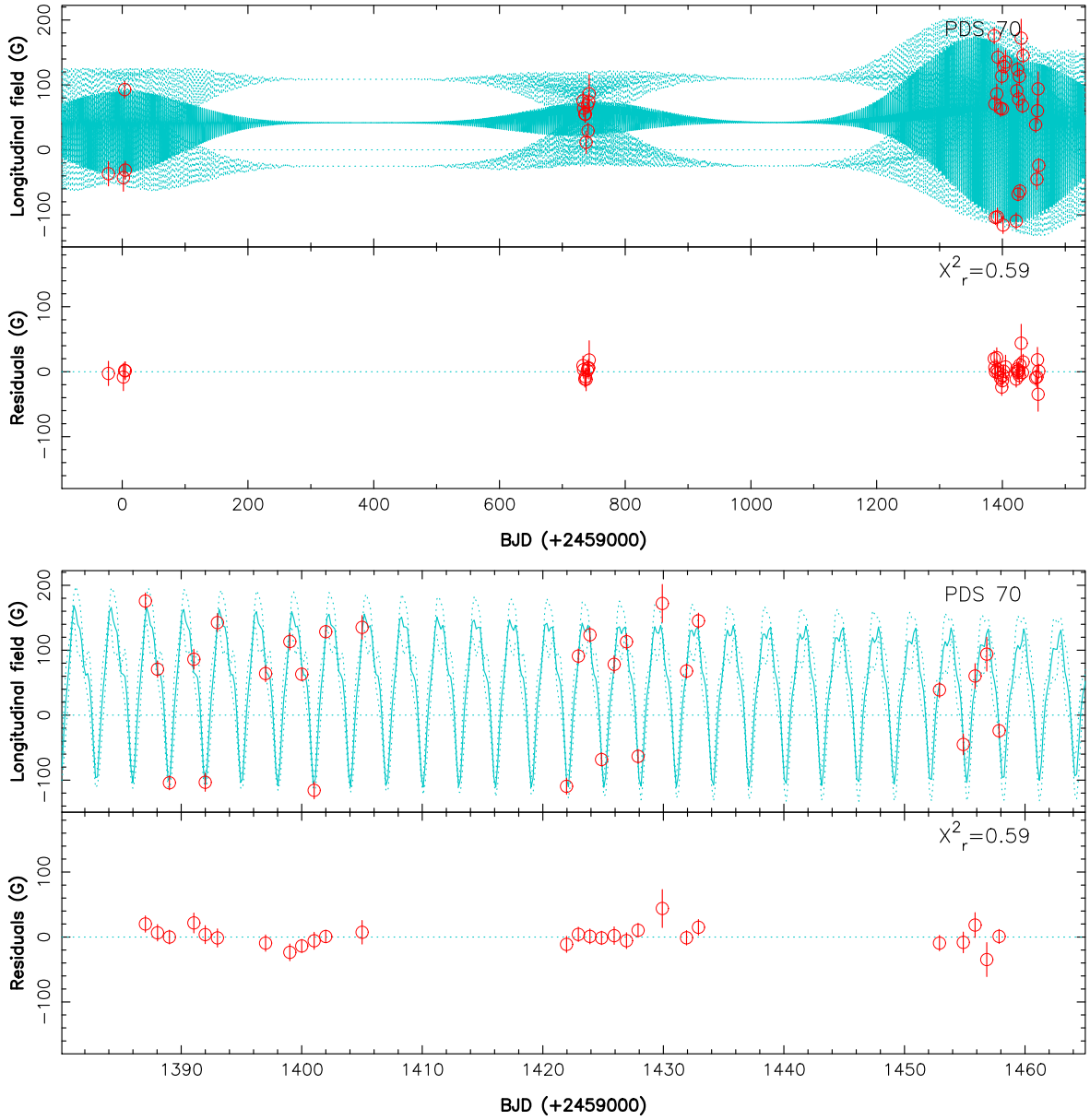

Figure 1. Longitudinal magnetic field B_ℓ of PDS 70 (red open circles) as measured with SPIRou, and QP GPR fit to the data (cyan full line) with corresponding 68 per cent confidence intervals (cyan dotted lines). The top panel shows the full data set, whereas the bottom panel is a zoom-on the 2024 (March to May) observations. The residuals, featuring an rms of 10.1 G ($\chi_r^2 = 0.59$), are shown in the bottom plot of each panel. The 3-d rotational modulation is clear in all seasons, especially in the last one where the amplitude of the modulation is largest.

our previous studies, i.e. by using quasi-periodic (QP) Gaussian Process Regression (GPR). This is achieved by finding out the hyperparameters of the covariance function that best describes our B_ℓ data, arranged in a vector denoted $\boldsymbol{y}$. The QP covariance function $c(t, t')$, we use in this purpose is as follows:

$$c(t,t') = \theta_1^2 \exp\left(-\frac{(t-t')^2}{2\theta_3^2} - \frac{\sin^2\left(\frac{\pi(t-t')}{\theta_2}\right)}{2\theta_4^2}\right), \quad (1)$$

where θ_1 is the amplitude (in G) of the Gaussian Process (GP), θ_2 its recurrence period (directly linked to $P_{\rm rot}$), θ_3 the evolution time-scale (in d) on which the shape of the B_ℓ modulation changes, and θ_4 a smoothing parameter describing the amount of harmonic complexity needed to describe the data (Haywood et al. 2014; Rajpaul et al. 2015). We then select the set of hyperparameters that yields the highest likelihood $\mathcal{L}$, defined by:

$$2\log\mathcal{L} = -n\log(2\pi) - \log|\boldsymbol{C}+\boldsymbol{\Sigma}+\boldsymbol{S}| - \boldsymbol{y}^T(\boldsymbol{C}+\boldsymbol{\Sigma}+\boldsymbol{S})^{-1}\boldsymbol{y}, \quad (2)$$

where $\boldsymbol{C}$ is the covariance matrix for our 40 epochs, $\boldsymbol{\Sigma}$ the diagonal variance matrix associated with $\boldsymbol{y}$, and $\boldsymbol{S} = \theta_5^2\boldsymbol{J}$ ($\boldsymbol{J}$ being the identity matrix) the contribution from an additional white noise source used as a fifth hyperparameter θ_5 (in case B_ℓ is affected by intrinsic variability beyond the photon noise described by our formal error bars). We then use a Monte Carlo Markov Chain (MCMC) process to

Table 2. Results of our MCMC modelling of the B_ℓ curve of PDS 70 with QP GPR. For each fitted hyperparameter, we list the derived value, the corresponding error bar and the assumed prior. Using a uniform prior (over an interval of 2.5–3.5 d) for the recurrence period virtually yields the same results. The knee of the modified Jeffreys prior is set to the median error bar of our B_ℓ measurements σ_B, equal to 13 G. We also quote the resulting χ^2_r and rms of the final GPR fit.

Parameter	Name	Value	Prior
Amplitude (G)	θ_1	70^{+15}_{-13}	Mod Jeffreys (σ_B)
Rec. period (d)	θ_2	3.008 ± 0.006	Gaussian (3.0, 0.2)
Evol. time-scale (d)	θ_3	100	Fixed
Smoothing	θ_4	0.30	Fixed
White noise (G)	θ_5	5^{+5}_{-3}	Mod Jeffreys (σ_B)
χ^2_r		0.59	Including photon noise only
Rms (G)		10.1	

explore the hyperparameter domain, yielding posterior distributions and error bars for each of them. We use here our MCMC and GPR modelling tools, as in our previous studies (e.g. Donati et al. 2023a, b, 2024a, b). The MCMC process is a conventional single chain Metropolis-Hastings scheme, typically carried out over a few 10^5 steps, including the first few 10^4 steps as burn-in, with convergence estimated from an autocorrelation analysis. The marginal logarithmic likelihood $\log \mathcal{L}_M$ of a given solution is computed using the approach of Chib & Jeliazkov (2001) as in, e.g. Haywood et al. (2014).

We started the exploration with all five hyperparameters free to vary, then ended up fixing θ_3 and θ_4, weakly constrained by our small set of observations, to the values (100 d and 0.3, see Table 2) yielding a marginal improvement in $\log \mathcal{L}$, with virtually no impact on the results and in particular on the derived $P_{\rm rot}$. This is due to both the small number of data points in any given season (limiting the achievable precision on θ_3) and the rather sparse sampling of the rotation cycle ($P_{\rm rot}$ being very close to a small integer number of days, limiting the precision on θ_4). The fit we obtain, shown in Fig. 1 and matching our data at a level of $\chi^2_r = 0.59$ (taking into account photon noise only and not θ_5), yields the hyperparameters listed in Table 2 and an estimate of $P_{\rm rot} = 3.008 \pm 0.006$ d. This value is consistent within error bars with the one derived from the same treatment of the ASAS-SN V- and g-band light curves (with all five hyperparameters free to vary), giving $P_{\rm rot} = 3.010 \pm 0.009$ d. The achieved precision on the derived rotation period only allows phase consistency to be ensured within a single season, as a result of both the temporal distribution of our data and the limited lifetime of the magnetic features at the surface of PDS 70 (see below).

We note that the full amplitude of the modulation of B_ℓ varied from season to season, being larger in 2024 (290 G) than in the two previous seasons and in 2022 in particular (70 G) where the Stokes V signatures were weak over a large fraction of the rotation cycle (see Section 5). The B_ℓ curve also changed in both shape and amplitude over the three SPIRou runs of 2024 (see bottom panel of Fig. 1). This seasonal magnetic evolution, only marginally significant when considering B_ℓ alone (θ_3 being only weakly constrained by our observations), is nonetheless clear from the temporal evolution of the LSD Stokes V profiles, as emphasized in Section 5. It tells us that the large-scale field of PDS 70 evolves with time as expected from a dynamo field, and does it on a time-scale of order of a few months, similar to (though not as fast as) what was reported for the other

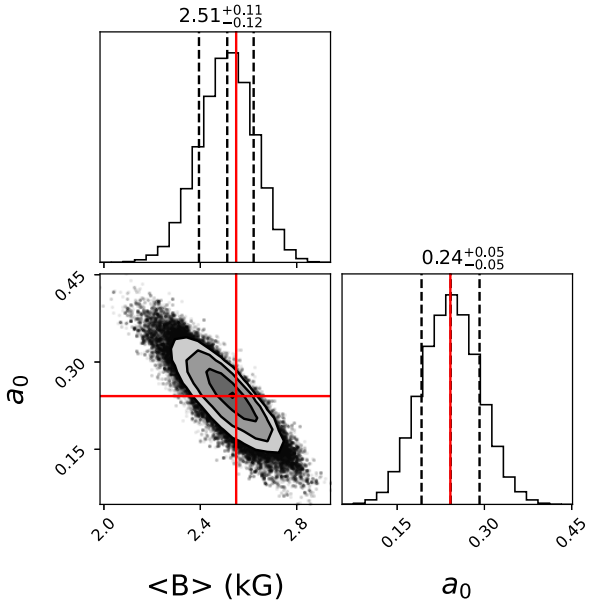

Figure 2. Magnetic parameters of PDS 70, derived by fitting our median SPIRou spectrum using the modelling approach of Cristofari et al. (2023a), which incorporates magnetic fields as well as an MCMC process to determine optimal parameters and their error bars. We find that PDS 70 hosts a small-scale magnetic field of $<B> = 2.51 \pm 0.12$ kG, whereas the relative area of non-magnetic regions is $a_0 = 24 \pm 5$ per cent, demonstrating a clear detection.

planet-hosting non-fully convective PMS star V1298 Tau (Finociety et al. 2023).

We finally looked at the Zeeman broadening of atomic and molecular lines with ZeeTurbo (Cristofari et al. 2023a, b) applied to our median spectrum of PDS 70, and find that four magnetic components, associated with small-scale magnetic fields of strengths 0, 2, 4, and 6 kG, and respective filling factors $a_0 = 24 \pm 5$ per cent, $a_2 = 45 \pm 7$ per cent, $a_4 = 11 \pm 7$ per cent, and $a_6 = 19 \pm 4$ per cent of the visible stellar surface, are needed to obtain a good match to the spectrum, yielding an overall small-scale field measurement of $<B> = 2.51 \pm 0.12$ kG for PDS 70 (see the derived corner plot of $<B>$ versus a_0 in Fig. 2). Adding more parameters in the modelling (i.e. for a 8 kG or even a 10 kG component) only marginally changes $<B>$ (by about 0.1 kG).

5 ZEEMAN–DOPPLER IMAGING

We analysed the Stokes I and V LSD profiles of PDS 70 using ZDI to simultaneously reconstruct the topology of the large-scale magnetic field and the distribution of brightness features at the surface of the star. Given the relatively fast temporal evolution of B_ℓ (see Section 4), we split our data into five subsets, respectively corresponding to epochs 2020 May–June, 2022 June, 2024 March, April and May, each gathering data collected over a few (2–9) rotation cycles. We stress again that the period of PDS 70, very close to a small integer number of days, does not allow one to easily obtain a dense sampling of the rotation cycle. This limitation is partly compensated by the relatively low limb darkening ($\simeq$0.4 in the H band, Claret, Diaz-Cordoves & Gimenez 1995) and the significant $v \sin i$, with each Doppler-broadened LSD profile yielding information about nine independent velocity strips across the stellar disc. As a result, we estimate that the spatial localization of brightness features is still reasonably accurate (typically 10° in longitude and 20° in latitude),

with most reconstructed features detected either as they cross the meridian or between two neighbouring phases of the rotation cycle. However, with only four spectra spread on about 40 per cent of the rotation cycle, the first of our five subsets is clearly too sparse to yield fully reliable ZDI maps. We nonetheless derived our results in the same way for all epochs, and discuss limitations whenever relevant.

For this study, we used the same ZDI code as in previous similar analyses of SPIRou data (e.g. Finociety et al. 2023; Donati et al. 2023a), which allows one to reconstruct the brightness distribution and the topology of the large-scale magnetic field at the surface of a rotating star from phase-resolved sets of Stokes *I* and *V* LSD profiles. This is performed through an iterative process, starting from a small magnetic field and a featureless brightness map and progressively adding information at the surface of the star, exploring the parameter space with a kind of conjugate gradient technique, until the modelled Stokes *I* and *V* profiles match the observed ones at the required level, usually $\chi^2_r \simeq 1$ (see e.g. Brown et al. 1991; Donati & Brown 1997; Donati et al. 2006, for more information on ZDI). As this inversion problem is ill-posed, ensuring a unique solution mandatorily requires regularization, which in our case follows the principles of maximum entropy image reconstruction (Skilling & Bryan 1984) to select the image featuring minimal information among those matching the data.

In practice, the surface of the star is described as a grid of 5000 cells, the spectral contributions of which are computed using Unno–Rachkovsky's analytical solution of the polarized radiative transfer equation in a plane-parallel Milne Eddington atmosphere (Landi degl'Innocenti & Landolfi 2004), with a local profile centred on 1750 nm and featuring a Doppler width and Landé factor of 3 km s^{-1} and 1.2, respectively (as in our previous studies, e.g. Donati et al. 2024b). By summing up the contributions of all grid cells, taking into account the star and cell characteristics and assuming the star rotates as a solid body, one can compute the synthetic profiles at the observed rotation cycles. Whereas the relative brightness at the surface of the star is simply described as a series of independent pixels, the large-scale magnetic field is expressed as a spherical harmonics expansion, using the formalism of Donati et al. (2006, see also Finociety & Donati 2022; Lehmann & Donati 2022; Donati et al. 2023a) in which the poloidal and toroidal components of the vector field depend on 3 sets of complex coefficients, $\alpha_{\ell,m}$ and $\beta_{\ell,m}$ for the poloidal component, and $\gamma_{\ell,m}$ for the toroidal component, where ℓ and m note the degree and order of the corresponding spherical harmonic term in the expansion. Given the significant $v \sin i$ of PDS 70, we used a spherical harmonic expansion with terms up to $\ell = 10$ in our study.

Before applying ZDI, all Stokes *I* LSD profiles of PDS 70 were corrected for the moderate veiling (see Section 7) by normalizing them to the same EW, while Stokes *V* profiles were scaled accordingly. Running ZDI on our five subsets, we obtained the fits shown in Fig. 3 and the brightness and magnetic maps depicted in Fig. 4. As a by product, we derived a measurement of $v \sin i$, equal to $v \sin i = 19.0 \pm 0.5$ km s^{-1}, slightly larger than the estimate of Thanathibodee et al. (2020) derived from much lower SNR HARPS spectra.

The recovered brightness maps only show low contrast features, as often the case for cool stars in the nIR (Finociety & Donati 2022; Finociety et al. 2023; Donati et al. 2024a) and in agreement with the Stokes *I* LSD profiles of PDS 70 exhibiting low level distortions only (see Fig. 3, top panel). The reconstructed features are nonetheless most likely real, given how they affect RVs (see Section 6) and how they repeatedly appear in the three independent images derived from the 2024 subsets. The low-latitude brightness inhomogeneities visible in these three maps around phase 0.75 (see Fig. 4) even suggest that differential rotation is likely present at the surface of PDS 70, progressively shifting these features to lower phases as time passes. The corresponding phase shift (0.1 cycle in a time-scale of 60 d) yields a differential rotation rate of order 10 mrad d^{-1} at lower latitudes with respect to the average rotation rate used to phase our data.[1] We come back on this point in Sections 6–8.

Regarding the magnetic topology, the ZDI results confirm our preliminary impression from the B_ℓ data that the large-scale field of PDS 70 evolves on a time-scale of a few months. We are indeed unable to fit with ZDI our complete data set over all seasons, nor a subset covering two consecutive seasons, nor even that including all our 2024 data, down to the same level of precision, unambiguously demonstrating that the magnetic topology of PDS 70 significantly evolved with time throughout our observing campaign. More specifically, the average strength of the field we recover varies from epoch to epoch by a factor of about 2.5×, from 160 to 395 G (see Table 3), with the weakest reconstructed field in 2022 June (when Stokes *V* signatures have low amplitudes for most of the rotation cycle, see Fig. 3) and the strongest in 2024 April. Note that given the limited phase coverage of our first subset, the corresponding large-scale field we retrieved, already the second strongest our our sample, is likely underestimated. The poloidal component of the field is dominant, always larger than 70 per cent and most of the time of order 90 per cent of the reconstructed magnetic energy. The dipole component of the poloidal field is the strongest, totalling between 46 per cent and 89 per cent of the poloidal field energy, and ranging between 200 G (in 2022) and about 400 G (in 2020 and 2024), with an average of 320 G over our observing epochs. As already pointed out from the B_ℓ curve (see Section 4), the evolution of the large-scale field in 2024 is significant, with the dipole inclination to the rotation axis varying by about 25° between March and April, and its strength increasing from 280 to 420 G before decreasing again to 300 G in May. Although some of this variation may reflect the different number of spectra in each subset and the limited sampling, we believe that most of it is real as the phase coverage is similar for all subsets (except the first one from 2020) given the value of $P_{\rm rot}$.

6 RV ANALYSIS

We derived RVs of PDS 70 from our SPIRou Stokes *I* profiles, to investigate in particular whether there may be close-in massive planets orbiting within a few 0.1 au of the host star, in addition to the two distant giant planets discovered by direct imaging (Keppler et al. 2018; Haffert et al. 2019). To measure RVs from Stokes *I* LSD profiles, we proceeded as in our study of V347 Aur (Donati et al. 2024c), i.e. by describing each individual LSD profile as a simple first-order Taylor expansion constructed from the median of all LSD profiles. This approach is similar to that used in the 'line-by-line' technique (Artigau et al. 2022), applied here to LSD profiles rather than to individual lines (not adequate for stars with large $v \sin i$'s experiencing accretion and veiling, see Section 7), and gives results that are slightly more precise and stable than a straightforward Gaussian fit to the LSD profiles. The derived RVs, ranging from 5.3 to 7.3 km s^{-1} with a median error bar of 0.16 km s^{-1} (see Table B1), exhibit an rms of 0.49 km s^{-1}, about 3× larger than the median error bar.

[1] A more quantitative analysis, with differential rotation used as a free ZDI parameter (as in, e.g. Donati, Collier Cameron & Petit 2003), is not possible in the present case given the sparse sampling of the rotation cycle and the strong intrinsic variability that the large-scale field of PDS 70 is subject to.

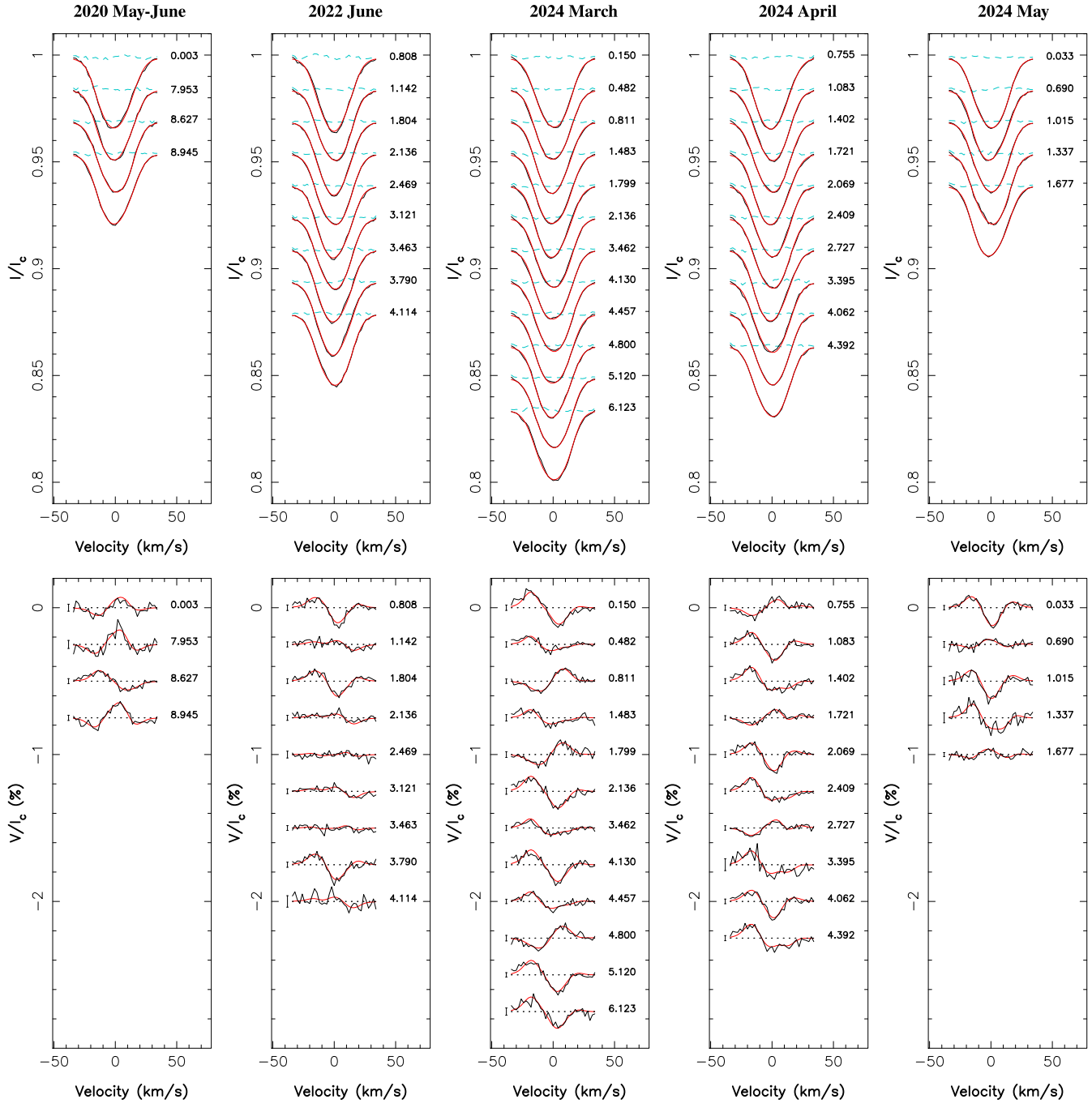

Figure 3. Observed (thick black line) and modelled (thin red line) LSD Stokes I (top row) and V (bottom row) profiles of PDS 70 for epochs 2020 May–June, 2022 June, 2024 March, April and May (left to right). Observed profiles were derived by applying LSD to our SPIRou spectra, using the atomic line mask outlined in Section 3. Rotation cycles (counting from 0, 250, 468, 479, and 490 for the five epochs, respectively, see Table B1) are indicated to the right of LSD profiles, while $\pm 1\sigma$ error bars are added to the left of Stokes V signatures. In the top row, we also show the differences between the observed and modelled LSD Stokes I profiles as cyan dashed lines.

A simple periodogram of our RV data (computed as in Press et al. 1992) confirms that rotational modulation dominates the RV fluctuations, with the strongest peak located close to $P_{\rm rot}$ and associated with a false alarm probability (FAP) of $\simeq$0.01 per cent (see top plot of Fig. C1 in Appendix C). Fitting now our RVs with QP GPR (as previously achieved for our B_ℓ data, see Section 4) confirms this result, yielding a period consistent with $P_{\rm rot}$ (3.00 ± 0.01 d) and a GP amplitude $\theta_1 = 0.41^{+0.12}_{-0.09}$ km s^{-1} for the rotational modulation, as well as filtered RVs (i.e. the difference between the raw RVs and the derived GP) whose rms of 0.24 km s^{-1} accounts for most of the excess RV dispersion (with respect to the median RV error bar of 0.16 km s^{-1}) but not for all ($\chi^2_{\rm r} = 2.08$, see Table 4). As the periodogram of the filtered RVs suggests that power remains at periods in the range 20–40 d with an FAP level of $\simeq$2 per cent (see the middle plot of Fig. C1), we repeated our QP GPR fitting, including this time an additional sine wave describing, e.g. the

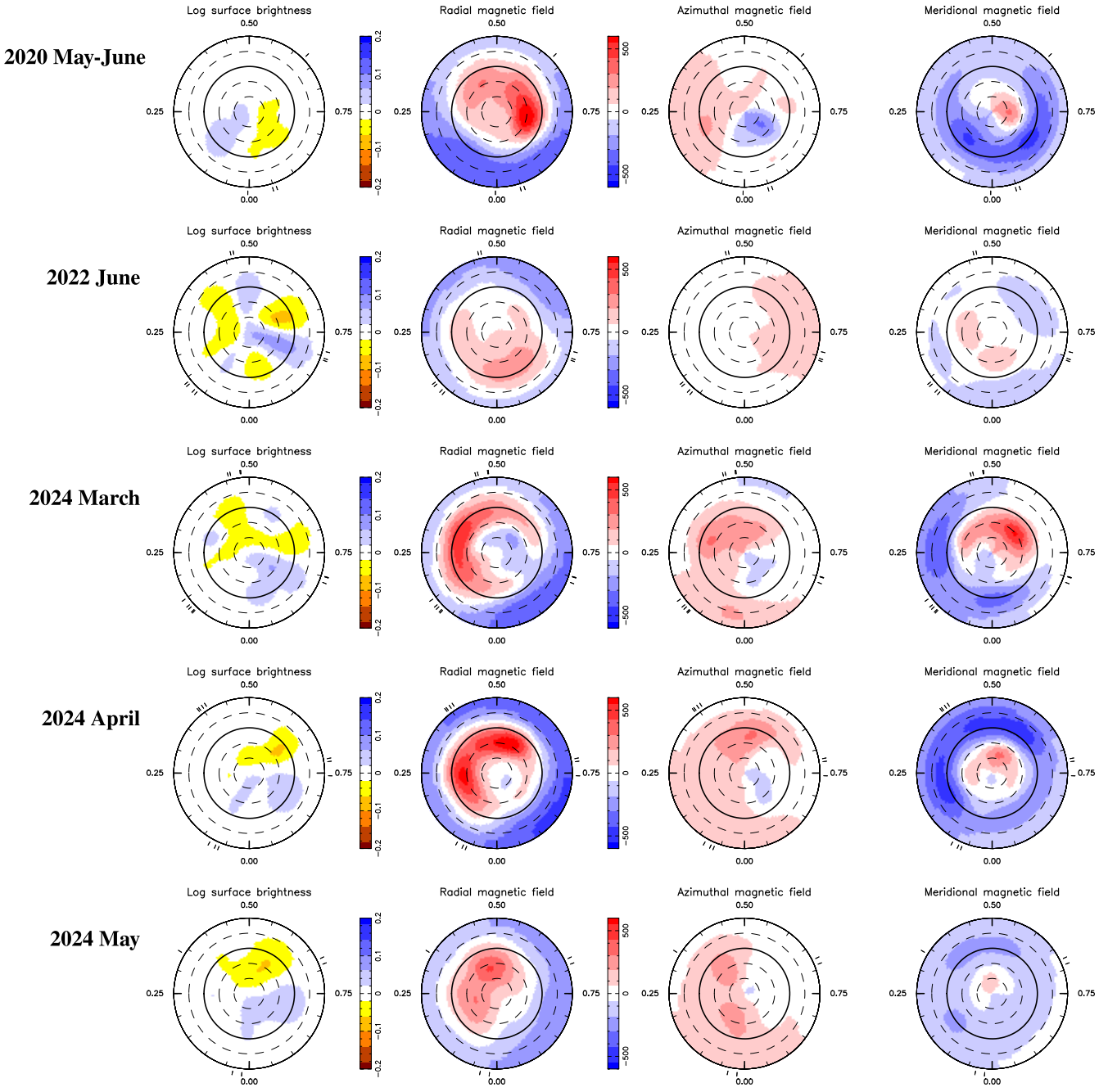

Figure 4. Reconstructed maps of the brightness and large-scale magnetic field of PDS 70 for epochs 2020 May–June, 2022 June, 2024 March, April and May (top to bottom), derived from the Stokes I and V LSD profiles of Fig. 3 using ZDI. In each row and from left to right, we show the logarithmic relative brightness with respect to the quiet photosphere, and the radial, azimuthal, and meridional field components in spherical coordinates (in G). All maps are shown in a flattened polar projection down to latitude -60°, with the north pole at the centre and the equator depicted as a bold line. Outer ticks indicate phases of observations. Bright and dark spots, respectively, appear as blue and yellow/orange features, whereas positive radial, azimuthal, and meridional fields, respectively, point outwards, counterclockwise, and polewards.

effect of a potential close-in planet in circular orbit around PDS 70, or that of another activity term fluctuating on a longer time-scale than $P_{\rm rot}$. We detect an RV signal on top of rotational modulation, at a period of $P_{\rm p} = 36.16 \pm 0.11$ d, with a semi-amplitude of $K_{\rm p} = 0.30^{+0.11}_{-0.08}$ km s^{-1} (i.e. at a level slightly below 4σ), which yields a significantly better fit to our RVs ($\chi^2_{\rm r} = 1.19$ and RV residuals, once both the GP and sinusoidal terms are subtracted, of 0.18 km s^{-1} rms, see Table 4). In both cases, two GPR hyperparameters, again weakly constrained by our sparse data (for the same reasons as in Section 4), were fixed to a given value yielding maximum log $\mathcal{L}_M$ in a preliminary run with all GPR variables free to vary, with virtually no difference on the outcome. The selected value for θ_4 is the same as that chosen for the modelling of B_ℓ though this parameter is usually smaller when adjusting RVs (e.g. Donati et al. 2023a), reflecting the limited precision (no better than 0.2) with which θ_4 can be estimated in PDS 70. The corresponding increase in marginal

Table 3. Properties of the large-scale magnetic field of PDS 70 for our five data subsets. We list the average reconstructed large-scale field strength $<B_V>$ (column 2), the polar strength of the dipole component B_d (column 3), the tilt of the dipole field to the rotation axis and the phase towards which it is tilted (column 4), and the amount of magnetic energy reconstructed in the poloidal component of the field and in the axisymmetric modes of this component (column 5). Error bars (estimated from variational analyses) are typically equal to 10 per cent for field strengths and percentages, 10° for field inclinations, and about twice worse for the first subset (for which ZDI is less reliable given the sparse phase coverage).

Data subset	$<B_V>$ (G)	B_d (G)	Tilt/phase (°)	Poloidal/axisym (per cent)
2020 May–June	345	395	37/0.59	93/67
2022 June	160	200	37/0.99	88/61
2024 March	320	280	57/0.32	71/57
2024 April	395	420	31/0.35	92/81
2024 May	245	300	33/0.34	86/70

log likelihood $\Delta \log \mathcal{L}_M = \log \mathrm{BF}$ reaches 5.6, suggesting that the detected medium-term RV signal is real (following Jeffreys 1961). The fit to the observed RVs as a function of time is depicted in Fig. 5 (with a zoom on the 2024 data in Fig. 6), whereas Fig. 7 shows the filtered RVs phase-folded on P_p. We note that the retrieved modulation period of the activity jitter is now slightly shorter than that reconstructed from B_ℓ data, again suggesting the presence of differential rotation at the surface of PDS 70. This agrees with our ZDI results of Section 5, with RVs being more sensitive to equatorial features whereas B_ℓ apparently probes a larger latitude range and thereby reflects an average rotation rate at a higher latitude (as in other TTSs, e.g. Donati et al. 2024b).

Given our sparse data, the detected medium-term RV signal shows multiple aliases (e.g. at periods of 38.2, 34.3, and 40.3 d), but with logarithmic Bayes factors log BF smaller by 0.5–1.0 than that of the peak signal at P_p (see Table 4). This signal is also present when considering the 2024 RV data alone, albeit with a lower significance ($\log \mathrm{BF} \simeq 4$) and a larger error on P_p ($\simeq$5 d), as expected from the lower number of points and the shorter time span of our observations. If this RV signal is of planetary origin, the candidate planet would have a minimum mass of $M_p \sin i = 4.5^{+1.7}_{-1.2} \mathrm{M}_\downarrow$, and hence a mass of $M_p = 5.2^{+2.0}_{-1.4}$ $\mathrm{M}_\downarrow$ if orbiting in the equatorial plane of the star. Located at a distance of 0.2 au, it would orbit within, and close to the inner edge of, the inner disc of PDS 70. Interpreting this RV signal in terms of a planet is however premature, first because our data are too sparse (with only 40 points altogether collected over a period of 1480 d) for such an analysis to be conclusive, secondly because P_p is close to one of the distant aliases of the synodic period of the Moon in the window function (SPIRou runs occurring in bright time).

To investigate this point in more depth, we looked at the bisector span (BIS) and the full width at half-maximum (FWHM) of our Stokes *I* LSD profiles of atomic lines (both listed in Table B1). We find that BISs are clearly anticorrelated with RVs (Pearson's coefficient $R = -0.8$), confirming that RVs are primarily affected by rotational modulation. A GPR fit to the BIS values (not shown) yields a dominant rotational modulation (with $\theta_1 = 0.8 \pm 0.2$ km s^{-1} and $\theta_2 = 3.000 \pm 0.008$ d), along with a lower amplitude signal ($K = 0.3 \pm 0.1$ km s^{-1}) at one of the previously mentioned aliases (40.3 ± 0.1 d) and a confidence level of $\log \mathrm{BF} = 5.6$. Performing again this analysis on FWHMs yields similar (though less precise) results, with clear rotational modulation ($\theta_1 = 0.6 \pm 0.2$ km s^{-1} and $\theta_2 = 3.02 \pm 0.04$ d), complemented by a signal ($K = 0.7 \pm 0.3$ km s^{-1}) of slightly lower significance ($\log \mathrm{BF} = 4.7$) at yet another alias of the longer period (32.3 ± 0.1 d). Both findings cast further doubts on the potential planetary origin of the detected RV signal at 36 d, and rather suggest that it may be attributable to activity fluctuations on a time-scale longer than P_{rot} (as those of B_ℓ and the parent large-scale field, see Sections 4 and 5). Besides, we note that FWHMs are in average smaller in 2022 (by about 1.2 km s^{-1}) than in 2020 and 2024, indicating that the small-scale field (like the large-scale one, see Section 5) was weaker at this intermediate epoch of our observations. We also find that RVs are not correlated with FWHMs, but rather to their first time derivative ($R \simeq 0.6$, as in, e.g. Donati et al. 2023a).

To gather additional clues on the origin of this enigmatic RV signal, we finally looked at the RVs derived from the Stokes *I* LSD profiles of CO lines (see Section 3 and Table B1). We find that these RVs are in average 0.45 km s^{-1} larger than those of atomic lines (convective downflows being relatively brighter for molecular than for atomic lines), and that they are less dispersed (with an rms of 0.34 km s^{-1}) as a result of CO lines being only sensitive to brightness features and not to magnetic fields. We also infer that these RVs are 35 per cent less precise than those of atomic lines (with a median error bar of 0.22 km s^{-1}, see Table B1), due to the smaller number of lines used for LSD (only partly compensated by the CO lines being narrower than atomic lines). We obtain that the activity jitter associated with rotational modulation is smaller for CO lines (with $\theta_1 = 0.26^{+0.10}_{-0.07}$ km s^{-1}) when fitting rotational modulation alone, yielding a residual rms of 0.21 km s^{-1}, and that an additional medium-term sinusoidal RV term is again needed to further improve $\log \mathcal{L}_M$ (by 8.9, see Table 4). However, the derived optimal period, now equal to $P_p = 28.19 \pm 0.11$ d, is hardly consistent with that obtained from the RVs, BISs, and FWHMs of atomic lines, and is even more suspicious, being quite close to one of the main 2-yr aliases of the synodic period of the Moon.

Since the medium-term RV fluctuation detected in addition to rotational modulation in the LSD profiles of both atomic and CO bandhead lines is apparently chromatic, and is also present in the BISs and FWHMs of atomic lines, we conclude that it is unlikely to be attributable to a candidate planet, but rather to activity at the surface of the star, e.g. caused by a change in the convective pattern resulting from the evolution of the large-scale magnetic field diagnosed in Sections 4 and 5, or within the inner disc regions. A similar dual-period magnetic modulation was recently detected in the B_ℓ curve of the young protostar V347 Aur (Donati et al. 2024c). Our study at least provides a conservative 3σ upper limit (of $\simeq$4 $\mathrm{M}_\downarrow$) on the minimum mass of a putative close-in giant planet in the inner disc of PDS 70, at a distance of about 0.2 au from the star.

7 ACCRETION AND WIND

To investigate accretion at the surface of PDS 70, we first looked at the spectral veiling, reducing the depth of spectral lines as a result of an added continuum (induced by accretion shocks at the surface of the star and by warm dust in the inner accretion disc, depending on wavelength). Veiling is measured from the EWs of the Stokes *I* LSD profiles of atomic lines (r_{JH}, in the *J* and *H* bands mostly) and of CO bandhead lines (r_K, in the *K* band), comparing them with those obtained for a couple of non-accreting T Tauri stars of similar spectral type (V819 Tau and TWA 9A) also observed with SPIRou. We find that r_{JH} is always smaller than 0.2, equal to 0.06 ± 0.06 in average, whereas r_K is significantly larger, equal to 0.5 ± 0.2 in average and reaching up to 1.2 (see Table B1). Both are correlated ($R \simeq 0.6$) and neither of them exhibits rotational modulation, rather showing sporadic peaks at apparently random epochs. Our estimates

Table 4. MCMC results for the two cases (activity only, activity plus putative planet) of our RV analysis of PDS 70, for atomic lines (columns 2 and 3) and for CO bandhead lines (columns 4 and 5). In each case, we list the recovered GP and putative planet parameters with their error bars, as well as the priors used whenever relevant. The last four rows give the χ^2_r and the rms of the best fit to our RV data, as well as the associated marginal logarithmic likelihood, $\log \mathcal{L}_M$, and marginal logarithmic likelihood variation, $\Delta \log \mathcal{L}_M = \log \mathrm{BF}$, with respect to the model without putative planet. Two GPR hyperparameters, weakly constrained by our sparse data, were fixed to a typical value yielding optimal results in a preliminary run with all GPR variables free to vary, with virtually no difference on the outcome.

	Atomic lines		CO bandhead		
Parameter	Activity only	Activity + planet	Activity only	Activity + planet	Prior
θ_1 (km s^{-1})	$0.41^{+0.12}_{-0.09}$	$0.44^{+0.14}_{-0.10}$	$0.26^{+0.10}_{-0.07}$	$0.21^{+0.08}_{-0.06}$	Mod Jeffreys ($\sigma_{\rm RV}$)
θ_2 (d)	3.00 ± 0.01	2.99 ± 0.01	3.00 ± 0.02	3.00 ± 0.02	Gaussian (3.0, 0.2)
θ_3 (d)	150	150	150	150	
θ_4	0.3	0.3	0.3	0.3	
θ_5 (km s^{-1})	$0.22^{+0.05}_{-0.04}$	$0.16^{+0.06}_{-0.04}$	$0.12^{+0.08}_{-0.05}$	$0.08^{+0.06}_{-0.04}$	Mod Jeffreys ($\sigma_{\rm RV}$)
$K_{\rm p}$ (km s^{-1})		$0.30^{+0.11}_{-0.08}$		$0.25^{+0.08}_{-0.06}$	Mod Jeffreys ($\sigma_{\rm RV}$)
$P_{\rm p}$ (d)		36.16 ± 0.11		28.19 ± 0.10	Gaussian (36.2 or 28.2, 0.3)
$T_{\rm c}$ (2459000 +)		731.9 ± 1.8		734.7 ± 1.7	Gaussian (732 or 735, 5)
$M_{\rm p} \sin i$ ($M_{\rm J}$)		$4.5^{+1.7}_{-1.2}$		$3.4^{+1.0}_{-0.8}$	Derived from $K_{\rm p}$, $P_{\rm p}$, and $M_\star$
χ^2_r	2.08	1.19	0.89	0.63	
Rms (km s^{-1})	0.24	0.18	0.21	0.18	
$\log \mathcal{L}_M$	−14.3	−8.7	−7.6	1.3	
$\log \mathrm{BF} = \Delta \log \mathcal{L}_M$	0.0	5.6	0.0	8.9	

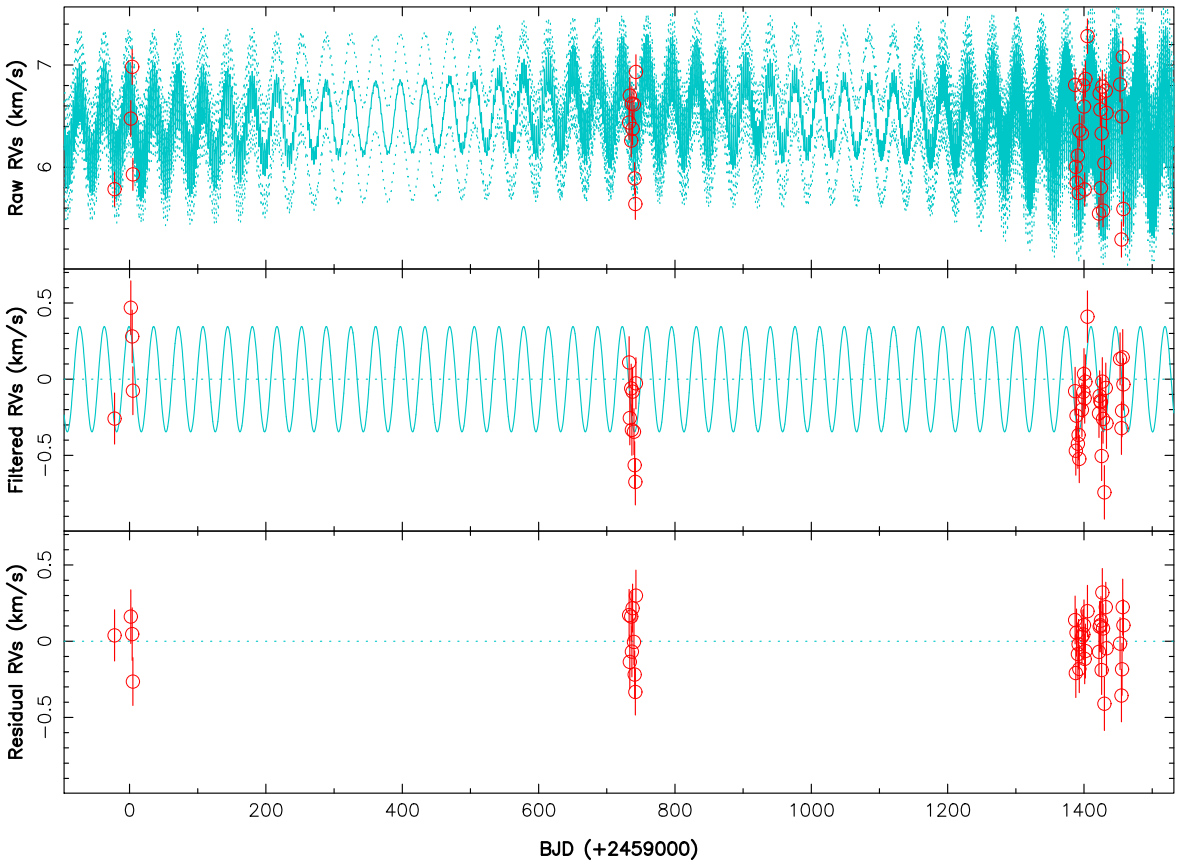

Figure 5. Raw (top), activity filtered (middle), and residual (bottom) RVs derived from atomic lines of PDS 70 (red open circles). The top plot shows the MCMC fit to the RV data, including a QP GPR modelling of the activity (cyan full line, with cyan dotted lines illustrating the 68 per cent confidence intervals), whereas the middle plot shows the RVs once activity is filtered out. A zoom on our 2024 data is shown in Fig. 6. Rotational modulation at $P_{\rm rot}$ dominates the dispersion of the raw RVs, especially in 2024 (see Fig. 6), whereas the additional medium-term fluctuation of the filtered RVs shown in the middle plot, also visible in the top plot, contributes to a smaller amount (see the text). The rms of the RV residuals is 0.18 km s^{-1}.

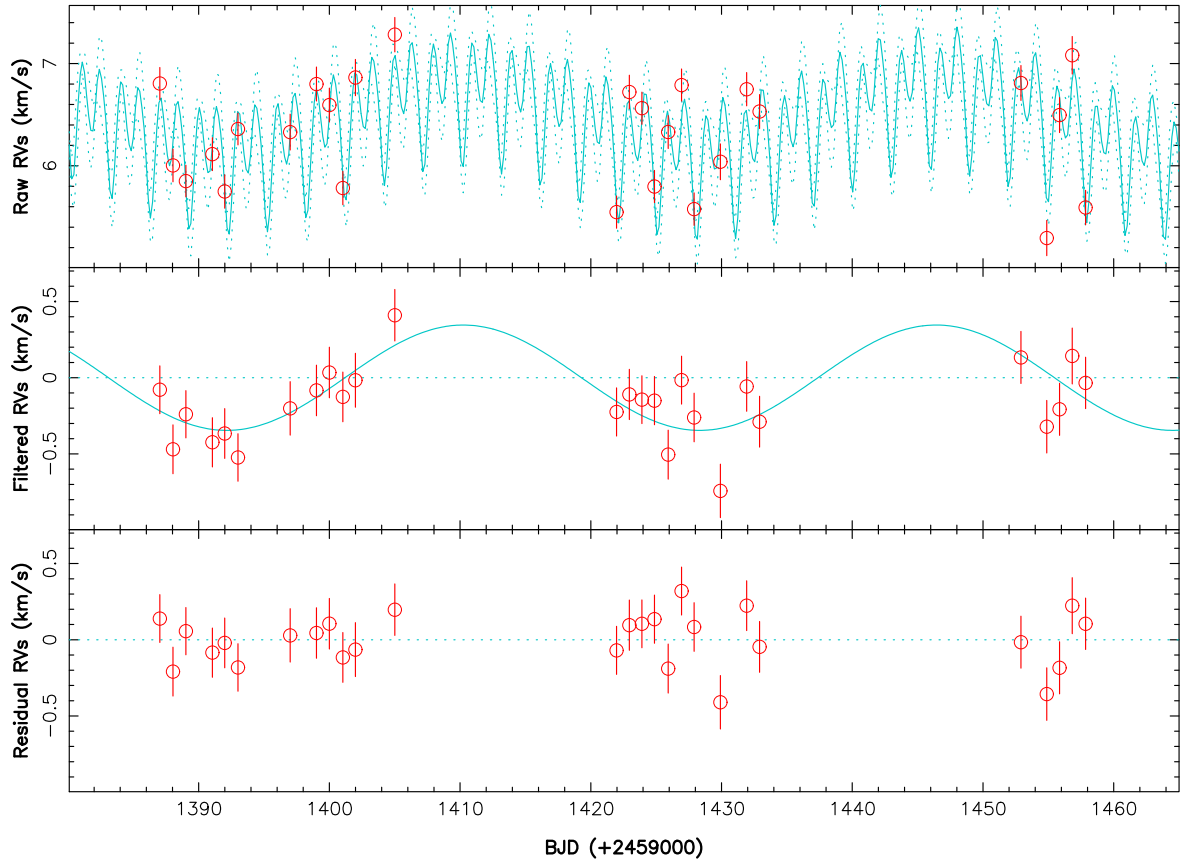

Figure 6. Same as Fig. 5, zooming on our 2024 data.

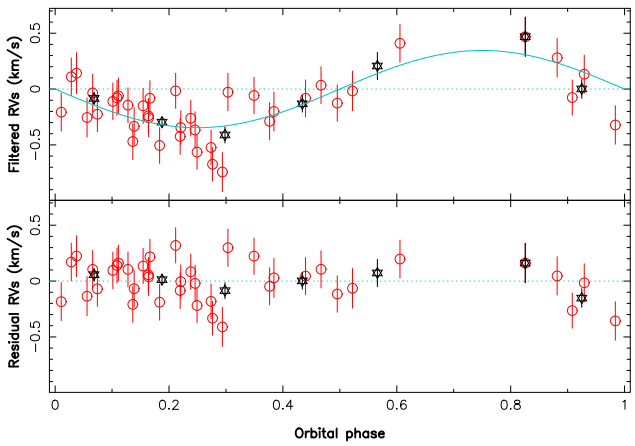

Figure 7. Filtered (top plot) and residual (bottom plot) RVs of atomic lines of PDS 70 phase-folded on $P_{\rm p}$. The red open circles are the individual RV points with the respective error bars, whereas the black stars are average RVs over 0.125 phase bins. As in Fig. 5, the dispersion of RV residuals is 0.18 km s^{-1}. Note the relative sparseness of points in the second half of the cycle, reflecting that $P_{\rm p}$ is close to one of the aliases of the synodic period of the Moon (SPIRou runs occurring in bright time).

are consistent with those of Sousa et al. (2023), derived from a subset of the same SPIRou spectra (with a different method).

The 1083-nm He I triplet is known to be an ideal proxy for investigating accretion and ejection flows of PMS stars and their surrounding discs, even those featuring low accretion rates like PDS 70 (Thanathibodee et al. 2020, 2022; Campbell-White et al. 2023). In PDS 70, both the blueshifted absorption and the redshifted emission components of the P-Cygni profile of the He I triplet exhibit drastic variability in time and shape over our observation campaign. In Fig. 8 (top-left panel), we show the stacked He I profiles of our 2024 observations, featuring a highly variable blueshifted absorption component extending at times down to -200 km s^{-1}, and a redshifted component in emission up to about 125 km s^{-1} (in the stellar rest frame) and in absorption beyond this velocity. We also detected a central narrow absorption component, putatively associated with chromospheric activity (Thanathibodee et al. 2022), and previously observed in Campbell-White et al. (2023) and Thanathibodee et al. (2022), but not in Thanathibodee et al. (2020).

The corresponding 2D periodogram (Fig. 8, bottom-left panel) shows significant power at 3.03 d (and its 29.5-d aliases), i.e. a period slightly larger than that derived from B_ℓ and RVs (see Sections 4 and 6) and in the redshifted absorption component only. This redshifted absorption presumably probes magnetospheric funnels regularly crossing the line of sight as the rotating star accretes material from the inner disc. We note that the periodicity detected in this absorption component, again slightly larger than $P_{\rm rot}$, is identical to that reported from the first *TESS* light curve (Thanathibodee et al. 2020; Gaidos et al. 2024), and likely relates to the rotation period of the high stellar latitudes at which accretion funnels are anchored, thus providing further evidence for differential rotation at the surface of PDS 70 (see Sections 5 and 6). Besides, both the red and blue wings of the central chromospheric absorption are also modulated with $P_{\rm rot}$, suggesting an RV variation of this contribution potentially

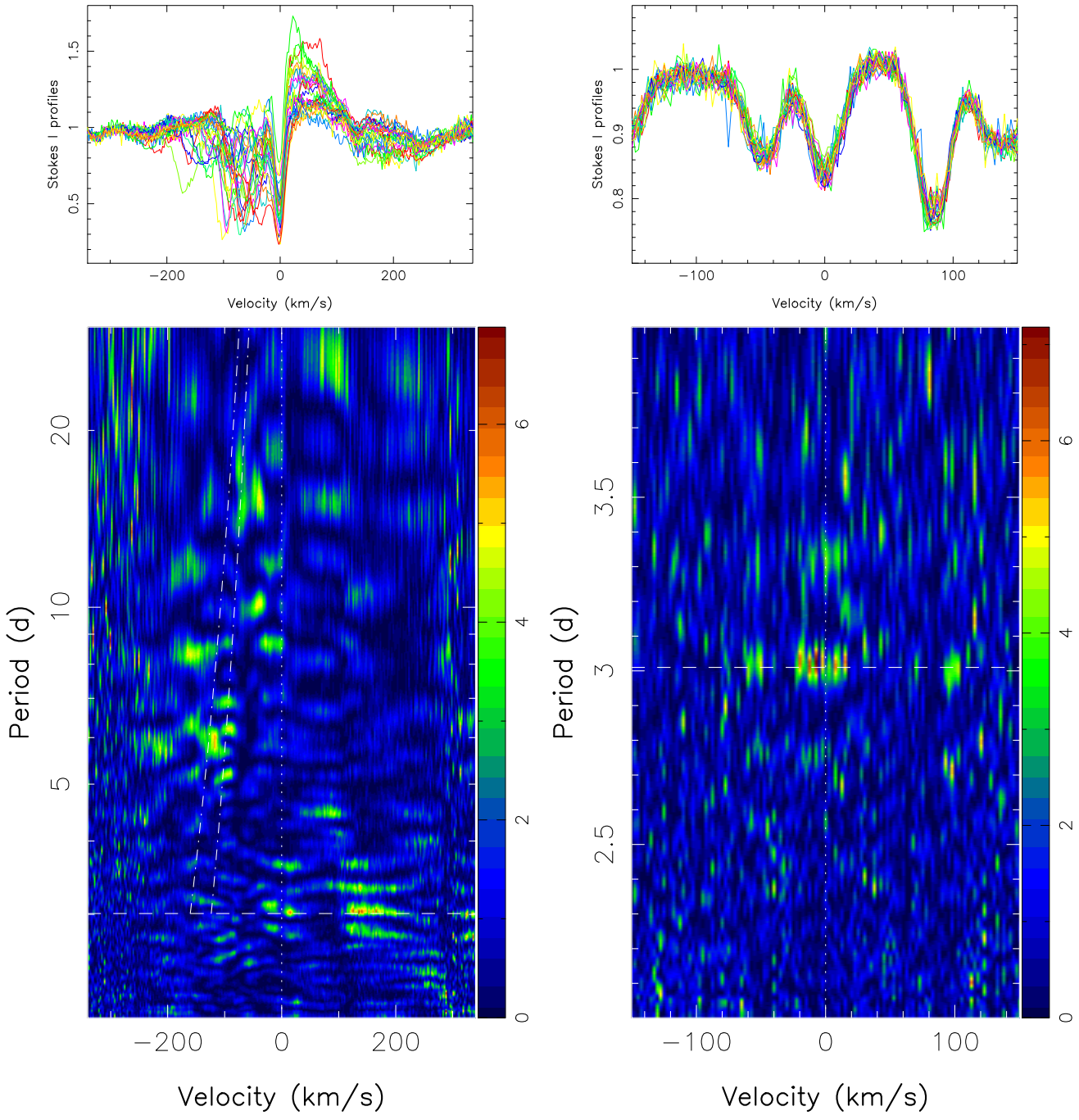

Figure 8. Stacked Stokes *I* profiles (top) and 2D periodograms (bottom) of the 1083.3-nm He I triplet (left) and the 1282.16-nm Paβ line (right), in the stellar rest frame, for our 2024 spectra of PDS 70. In both periodograms, the dashed horizontal line traces $P_{\rm rot}$. The slanted dot–dashed lines in the left panel illustrate how the Keplerian velocity and its line-of-sight projection vary as a function of the Keplerian period beyond $r_{\rm cor}$ in the inner disc. The colour scale depicts the logarithmic power. We caution that only the main peaks (coloured yellow to red and extending over at least several velocity bins) are likely to be real in these plots.

tracing a low-latitude chromospheric region at the surface of the star. No Zeeman signature is detected in conjunction with this central component, confirming that it is unlikely related to the high-latitude footpoints of funnel flows linking the star to the inner edge of the disc (conversely to what was found on, e.g. TW Hya, Donati et al. 2024b).

The blueshifted absorption, likely probing a wind from the inner disc (Thanathibodee et al. 2022; Campbell-White et al. 2023) given its shape and temporal variability (Edwards et al. 2003; Kwan, Edwards & Fischer 2007), exhibits distributed power at periods longer than $P_{\rm rot}$, ranging from from 5 to 20 d (see Fig. 8) and corresponding to Keplerian periods at distances of 0.055 to 0.14 au. We speculate that these features reflect azimuthal structures in the inner disc wind of PDS 70, possibly probing magnetically active regions where the wind is stronger and potentially linked to the magnetically driven wind traced with the 630-nm [O I] (originating

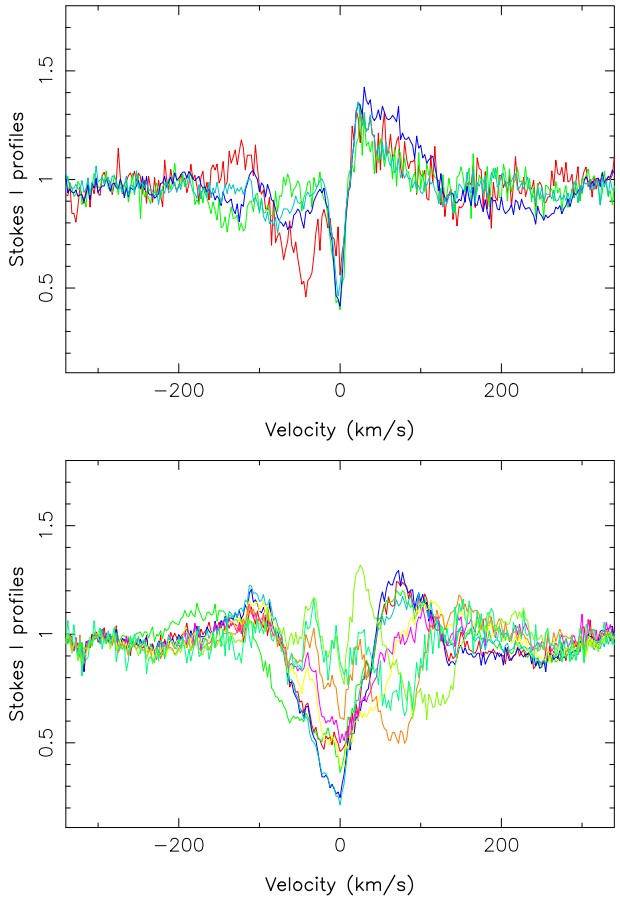

Figure 9. Same as top-left panel of Fig. 8, for our 2020 (top) and 2022 (bottom) He I spectra of PDS 70. The three profiles in the bottom panel showing strong redshifted absorption at velocities 50−150 km s^{-1} correspond to the last three spectra collected in 2022 June.

from the same region of the inner disc, Campbell-White et al. 2023). We note a potential trend for longer periods to show up at smaller blue shifts, suggesting disc wind outward velocities scaling with Keplerian velocities in the disc (Blandford & Payne 1982; Thanathibodee et al. 2022), decreasing from 135 to 85 km s^{-1} for periods in the range 5–20 d in PDS 70. Finally, we see no clear periodic modulation in the red-shifted emission component between 0 and 120 km s^{-1}, presumably probing the top part of accretion funnels close to $r_{\rm cor}$. This suggests that accretion flows from the inner disc to the star are likely to be unsteady, i.e. irregular from one rotation cycle to the next, as redshifted emission would otherwise be expected to exhibit some level of rotational modulation as accretion columns rotate around the star.

We also present in Fig. 9, the He I triplet profiles of PDS 70 during our 2020 and 2022 observations, showing a behaviour similar to that of our 2024 observations with the exception of the redshifted emission component up to 125 km s^{-1} that switched to absorption in the last 3 spectra collected in June 2022, as described in previous studies Thanathibodee et al. (2020, 2022). This supports our previous conclusion that accretion flows from the inner disc are unsteady in PDS 70, featuring sporadic episodes of stronger absorption from the inner disc like the one which occurred during our last three observations of 2022 June. We stress that this episode of enhanced accretion occurred at an epoch where the large-scale field of PDS 70 is significantly smaller than average (see Section 5).

We find that Paβ in PDS 70 shows very little temporal variability (see top-right panel of Fig. 8 for our 2024 observations). The corresponding 2D periodogram (bottom-right panel) shows that this variability is modulated with $P_{\rm rot}$ and confined to a velocity range of $\pm v \sin i$ (as for the neighbouring Ca I and Ti I lines on the left and the right of Paβ respectively, but with significantly more power). This variability is most likely of chromospheric origin, as for the central absorption component of He I. The modulated component of Paβ amounts to a peak-to-peak EW variation of about 0.4 km s^{-1} (1.7 pm). The Paβ profiles of PDS 70 in our 2020 and 2022 observations were very similar to those in 2024, with variations from epoch to epoch comparable to the modulation detected in 2024. Besides, we find that the EW of Paβ in PDS 70 is equal to 5.6 ± 0.4 km s^{-1} (24 ± 2 pm) at all epochs (even in our last three spectra of 2022 June), i.e. identical within error bars to that in our comparison weak-line TTSs V819 Tau and TWA 9A. Using the scaling laws reported between emission line fluxes and accretion luminosities of accreting TTSs (Alcalá et al. 2017), this would imply a 3σ upper limit on $\log \dot{M}$ of -11 (in M$_\odot$ yr^{-1}) at the surface of PDS 70, much lower than the reported values (of order -10, Thanathibodee et al. 2020; Campbell-White et al. 2023; Gaidos et al. 2024) that should imply Paβ EW differences (with respect to non-accreting TTSs) and/or temporal variations of order 4 km s^{-1} (17 pm), i.e. 10× larger than those we observed. That we do not see excess Paβ flux beyond velocities of $\pm v \sin i$ is further evidence that whichever weak mass accretion rate is occurring on PDS 70 is undetected in the Paβ profiles of our SPIRou spectra despite the relatively high SNR. The same conclusion holds for Brγ, for which no variability (from either chromospheric activity or accretion) is observed within the line profile nor beyond velocities of $\pm v \sin i$, and with an average (veiling corrected) EW of 1.8 ± 0.5 km s^{-1} (13 ± 4 pm) in PDS 70 that is only marginally different (by 0.8 ± 0.5 km s^{-1} or 6 ± 4 pm) from that in our comparison non-accreting TTSs. It yields again a 3σ upper limit on $\log \dot{M}$ of -11 (in M$_\odot$ yr^{-1}) at the surface of PDS 70 using the scaling laws of Alcalá et al. (2017). A potential explanation for this discrepancy is that PDS 70 was in a state of particularly low accretion rate at the various epochs of our observations. More likely, we suspect that the scaling laws of Alcalá et al. (2017), whose average precision is about a factor of 3 on accretion luminosities derived from Paβ and Brγ fluxes, may be less accurate or more dispersed for logarithmic accretion luminosities (relative to L$_\odot$) in the range -3 to -4 of relevance for PDS 70, being based on a comparatively larger number of upper limits than for larger accretion luminosities.

Using the previously published logarithmic mass accretion rate along with our estimates of the dipole component of the large-scale field of PDS 70 (see Section 5), we computed the distance $r_{\rm mag}$ at which the field is able to disrupt the inner disc, using simulation results of magnetospheric accretion (Zanni & Ferreira 2013; Blinova, Romanova & Lovelace 2016; Blinova et al. 2019; Pantolmos, Zanni & Bouvier 2020) and in particular the analytical expression of Bessolaz et al. (2008) based on such simulations and confirmed in newer ones. For $\log \dot{M}$ between -9.7 and -10.3 (in units of M$_\odot$ yr^{-1}, see Table 1), we find that $r_{\rm mag}$ ranges from 5.6 to 8.3 $R_\star$ for the strongest dipole field we measured on PDS 70 (420 G, see Table 3), and from 3.7 to 5.4 $R_\star$ for the weakest dipole field (200 G). This implies $r_{\rm mag}/r_{\rm cor} = 1.08 \pm 0.21$ in the strong field case and $r_{\rm mag}/r_{\rm cor} = 0.70 \pm 0.14$ in the weak field one, or $r_{\rm mag}/r_{\rm cor} = 0.92 \pm 0.18$ for an intermediate case (corresponding to 320 G, i.e. the average dipole field of PDS 70). It confirms in

particular that the inner edge of the inner disc of PDS 70 is in average located close to $r_{\rm cor}$, moving towards the star at epochs of weaker dipole field (as in 2022 June) or extending beyond $r_{\rm cor}$ at epochs of stronger dipole field (as in 2024 April or 2020 May and June). Whereas most disc material is expected to be accreted onto the star in the weaker field case, a magnetic propeller mechanism (Romanova et al. 2004; Ustyugova et al. 2006) can be triggered in the strong field case where a smaller amount of disc material is accreted onto the star, leading to variations of $\log \dot{M}$ and sporadic eruptive episodes (D'Angelo & Spruit 2012; Zanni & Ferreira 2013).

8 SUMMARY, DISCUSSION AND CONCLUSION

In this paper, we report spectropolarimetric and velocimetric observations of the weakly accreting, planet hosting T Tauri star PDS 70, collected with SPIRou at CFHT in 2020 May–June, 2022 June, and 2024 March–May. We detect clear Zeeman signatures in the LSD Stokes V profiles of PDS 70, implying longitudinal magnetic fields B_ℓ ranging from -116 to 176 G and modulated with the average stellar rotation period of $P_{\rm rot} = 3.008 \pm 0.006$ d, consistent with the recurrence period derived from the archival ASAS-SN V- and g-band light curves of PDS 70. Splitting our LSD Stokes I and V profiles into five subsets corresponding to different epochs (three of which in 2024), we reconstructed the brightness and magnetic maps of PDS 70 and their changes with time. We find that PDS 70 hosts a large-scale magnetic field that evolves with time on a time-scale of a few months, with a dominant dipole component varying from 200 (in 2022) to about 400 G (in 2020 and 2024), with an average of 320 G. Our 2024 observations, spread over 3 months, show clear month-to-month changes in the large-scale field topology, both in the orientation and strength of the dipole field. The magnetic topology of PDS 70 is consistent with those of partly convective TTSs, often showing weaker and more rapidly varying fields than fully convective ones (Donati & Landstreet 2009). From the broadening of spectral lines in our median spectrum, we find that PDS 70 hosts a small-scale field of 2.51 ± 0.12 kG, typical to that of TTSs (e.g. Johns-Krull 2007; López-Valdivia et al. 2021). We also infer that FWHMs of atomic lines are smallest in 2022, indicating that the small-scale field of PDS 70 was weaker at this intermediate epoch than in 2020 and 2024.

Our observations also suggest that the surface of PDS 70 is likely sheared by latitudinal differential rotation, with the pole rotating more slowly than the equator. RVs, more sensitive to low-latitude surface inhomogeneities, indicate recurrence periods down to 2.99 d, whereas the redshifted absorption component of the He I line, probing magnetospheric funnels anchored at high stellar latitudes, points to a longer rotation period of 3.03 d. It implies a level of differential rotation between the low and high latitudes of $\simeq$28 mrad d^{-1}, about half that at the surface of the Sun. This is again typical to non-fully convective stars, often exhibiting differential rotation rates larger than fully convective ones, even at rotation rates much larger than that of the Sun (e.g. Donati & Landstreet 2009).

We also investigated whether PDS 70 hosts a close-in giant planet in addition to the two distant ones already revealed by direct imaging (Haffert et al. 2019). We find that RVs derived from atomic lines of PDS 70 exhibit variability at an rms level of 0.49 km s^{-1}, featuring time-dependent rotational modulation with an average semi-amplitude of 0.44 km s^{-1} as a result of brightness and magnetic regions at the surface of the star. Besides, we show that RVs from the CO bandhead lines in the K band, insensitive to magnetic fields, are also rotationally modulated with a twice weaker amplitude, reflecting the impact of surface brightness inhomogeneities on the RV curve of PDS 70. RVs from both atomic and CO lines are apparently also fluctuating on a longer time-scale of about 28−36 d (with semi-amplitudes of 0.30 and 0.25 km s^{-1} respectively), but most likely as a result of activity rather than of a putative close-in giant planet around PDS 70 given that BISs and FWHMs of LSD Stokes I profiles of atomic lines are also showing a similar variation pattern. We derive a 3σ upper limit of $\simeq$4 $M_\oplus$ for the minimum mass of a close-in planet at a distance of about 0.2 au. The physical nature of this activity is currently unclear. Whereas the period on which it fluctuates may suggest it originates from the inner disc at a distance of $\simeq$0.2 au, i.e. in a region from which a magnetically driven wind is launched (Campbell-White et al. 2023), the RV fluctuation it generates (of semi-amplitude 0.25−0.30 km s^{-1}) rather argues in favour of a stellar phenomenon (e.g. granulation) given both the low density of the inner disc and the magnitude of the spectral contribution required to induce such a perturbation.

We examined the usual accretion proxies and their temporal variations in the spectrum of PDS 70, and in particular the 1083.3-nm He I triplet of PDS 70 known to be a very sensitive probe of magnetospheric accretion towards the host star and of magnetically driven winds from the inner accretion disc. We find that the He I profiles of PDS 70 show both blueshifted and redshifted extended absorption, bracketing a redshifted emission component and a narrow central (likely chromospheric) absorption feature. Only the extended redshifted and the central chromospheric components exhibit rotational modulation, the former likely reflecting accretion funnels periodically crossing the line of sight as PDS 70 rotates. This modulation of the redshifted He I absorption component confirms that accretion still takes place at the surface of PDS 70. Power at periods ranging from 5 to 20 d is detected in the blueshifted absorption component at velocities ranging down to -150 km s^{-1}, potentially tracing azimuthal structures in the inner disc wind of PDS 70, e.g. from magnetic regions of the disc where the wind is stronger. These structures may be the anchor points of the magnetically driven wind traced with the 630-nm [O I] (originating from the same region of the inner disc, Campbell-White et al. 2023).

Only chromospheric activity (inducing rotational modulation of the line EW at a level of a few pm within velocities of $\pm v \sin i$) but no sign of accretion (within and beyond $\pm v \sin i$) is detected in Paβ down to EWs of $\pm$0.4 km s^{-1}, whereas Brγ shows no clear sign of either. Using the scaling relations linking Paβ and Brγ line fluxes to accretion luminosities (e.g. Alcalá et al. 2017), we infer a 3σ upper limit on $\log \dot{M}$ of -11 (in $M_\odot$ yr^{-1}) at the surface of PDS 70. It either suggests that PDS 70 was in a state of unusually low accretion rate during all of our observations, or more realistically, that the scaling relations of Alcalá et al. (2017), yielding accretion luminosities from Paβ and Brγ line fluxes, may be less accurate and more dispersed at the low accretion rates reported for PDS 70.

Given the published accretion rate and the large-scale magnetic topology derived from our study, we can conclude that PDS 70 is apparently able to disrupt the inner accretion disc up to an average distance (relative to $r_{\rm cor}$) of $r_{\rm mag}/r_{\rm cor} = 0.92 \pm 0.18$ (the error bar reflecting the reported range of $\log \dot{M}$), with extreme values spanning from 0.70 ± 0.14 to 1.08 ± 0.21 at epochs of weakest and strongest dipole field components, respectively. This variation of the large-scale field can in particular qualitatively explain fluctuations in the accretion rate at the surface of PDS 70, with most of the disc material being accreted onto the star through conventional magnetospheric accretion patterns when the dipole field is on the weak side (as in 2022 June), or only a small fraction of it reaching the stellar surface when the dipole field is strongest and the accretion mode switches

to a magnetic propeller regime (Romanova et al. 2004; Ustyugova et al. 2006; D'Angelo & Spruit 2012; Zanni & Ferreira 2013).

Comparing with the ASAS-SN g-band light curve (see Fig. A1), we find that PDS 70 is in average fainter when the small-scale field and the dipole component of the large-scale magnetic field are weaker, i.e. in 2022 June, also coinciding with PDS 70 being brighter at 3.4 and 4.6 μm (Gaidos et al. 2024). These photometric changes apparently result from occultation by sub-μm dust from the inner disc dimming the star at optical wavelengths and generating additional 3−5 μm emission (Gaidos et al. 2024). This leads us to speculate that dust is likely able to pile up at $r_{\rm cor}$ when the dipole component of the large-scale field is strong enough to ensure that $r_{\rm mag}$ extends up $r_{\rm cor}$ (as proposed by Sanderson et al. 2023), like in our 2020 and 2024 SPIRou observations. In such cases, PDS 70 suffers less occultation and less reddening, with dust clouds located at $r_{\rm cor}$ in the disc plane only marginally intersecting the line of sight given the viewing angle, and the optical light curves tends to be periodic and reflect mostly stellar activity. As dust clouds at $r_{\rm cor}$ also rotate with $P_{\rm rot}$ and are stable against gravity, the light curve can at times feature a 'scallop-shell' morphology like that collected by *TESS* in sector 11 when dust clouds happen to occult a larger fraction of the stellar disc. On the opposite, when the dipole component of PDS 70 gets weaker and $r_{\rm mag}$ is significantly smaller than $r_{\rm cor}$, dust is able to penetrate the magnetosphere and to occult the stellar disc more substantially, generating lower average optical fluxes and larger amplitude stochastic light curves like those collected by *TESS* in sectors 38 and 65 as dust within the magnetosphere rapidly drifts towards the star being no longer supported against gravity. Our scenario is at least able to qualitatively reconcile our observations with those of Gaidos et al. (2024), despite their conclusions differing from ours on how magnetic fields drive the process.

Our study demonstrates the key value of repeated spectropolarimetric and velocimetric observations of the PMS planet-hosting star PDS 70 carried out over multiple seasons, like those we secured with SPIRou, to further characterize the central star and the inner accretion disc, the magnetospheric accretion processes linking both and the wind escaping from the disc, as well as any planet that may hide within 1 au of the host star. With its two outer giant planets, PDS 70 is an ideal target to investigate whether more such planets can also be present at smaller orbital distances, e.g. after undergoing inward migration over the last few Myr since their initial formation beyond the snow line. Even though we were only able to obtain an upper limit on the mass of such a putative close-in giant planet at 0.2 au with the present study, regular observations carried out over a longer time span of about a decade should be able to reach a more definite conclusion on this point up to distances of a few au's, and provide at the same time essential information on the temporal evolution of the large-scale magnetic field of the host star, on how this evolving field impacts the way material is accreted from the disc, and on the properties of the magnetically driven wind escaping from the central disc regions. We thus strongly advocate for renewed SPIRou observations of PDS 70 in forthcoming seasons, in particular at epochs where complementary data on a wider wavelength domain can be collected (e.g. with ASAS-SN, *TESS*, and ESPaDOnS at CFHT, and HARPS and X-Shooter at ESO).

ACKNOWLEDGEMENTS

We thank an anonymous referee for valuable comments on an earlier version of our manuscript. This project received funds from the European Research Council (ERC) under the H2020 and Horizon Europe research & innovation programs (grant agreement no. 740651 NewWorlds, no. 742095 SPIDI, no. 101053020 Dust2Planets, no. 101039452 WANDA), from the Agence Nationale pour la Recherche (ANR, project ANR-18-CE31-0019 SPlaSH) and from the Investissements d'Avenir program (project ANR-15-IDEX-02), and was also supported by the NKFIH excellence grant TKP2021-NKTA-64. SHPA acknowledges financial support from CNPq, CAPES, and FAPEMIG. This work benefitted from the SIMBAD CDS database at URL http://simbad.u-strasbg.fr/simbad, the ADS system at URL https://ui.adsabs.harvard.edu, and the ASAS-SN archival photometry http://asas-sn.osu.edu. Our study is based on data obtained at the CFHT, operated by the CNRC (Canada), INSU/CNRS (France), and the University of Hawaii. The authors wish to recognize and acknowledge the very significant cultural role and reverence that the summit of Maunakea has always had within the indigenous Hawaiian community. We are most fortunate to have the opportunity to conduct observations from this mountain.

DATA AVAILABILITY

SLS data are publicly available from the Canadian Astronomy Data Center, whereas SPICE data will be available at the same place by mid 2025.

REFERENCES

Alcalá J. M. et al., 2017, A&A, 600, A20
André P., Di Francesco J., Ward-Thompson D., Inutsuka S. I., Pudritz R. E., Pineda J. E., 2014, in Beuther H., Klessen R. S., Dullemond C. P., Henning T.eds, Protostars and Planets VI. University of Arizona Press, Tucson, AZ, p. 27
Artigau É. et al., 2022, AJ, 164, 84
Baraffe I., Homeier D., Allard F., Chabrier G., 2015, A&A, 577, A42
Benisty M. et al., 2021, ApJ, 916, L2
Bessolaz N., Zanni C., Ferreira J., Keppens R., Bouvier J., 2008, A&A, 478, 155
Blakely D. et al., 2024, preprint (arXiv:2404.13032)
Blandford R. D., Payne D. G., 1982, MNRAS, 199, 883
Blinova A. A., Romanova M. M., Lovelace R. V. E., 2016, MNRAS, 459, 2354
Blinova A. A., Romanova M. M., Ustyugova G. V., Koldoba A. V., Lovelace R. V. E., 2019, MNRAS, 487, 1754
Bouvier J., 2022, in The 21st Cambridge Workshop on Cool Stars, Stellar Systems, and the Sun, p. 40, https://coolstars21.github.io/
Braun T. A. M., Yen H.-W., Koch P. M., Manara C. F., Miotello A., Testi L., 2021, ApJ, 908, 46
Brown S. F., Donati J.-F., Rees D. E., Semel M., 1991, A&A, 250, 463
Cabrit S., 2024, in EAS2024, Session SS5. p. 2674
Campbell-White J. et al., 2023, ApJ, 956, 25
Chambers J., 2018, ApJ, 865, 30
Chib S., Jeliazkov I., 2001, J. Am. Stat. Assoc., 96, 270
Claret A., Diaz-Cordoves J., Gimenez A., 1995, A&AS, 114, 247
Cristofari P. I. et al., 2023a, MNRAS, 522, 1342
Cristofari P. I. et al., 2023b, MNRAS, 526, 5648
D'Angelo C. R., Spruit H. C., 2012, MNRAS, 420, 416
David T. J., Petigura E. A., Luger R., Foreman-Mackey D., Livingston J. H., Mamajek E. E., Hillenbrand L. A., 2019, ApJ, 885, L12
Donati J.-F., Brown S. F., 1997, A&A, 326, 1135
Donati J., Landstreet J. D., 2009, ARA&A, 47, 333
Donati J.-F., Semel M., Carter B. D., Rees D. E., Collier Cameron A., 1997, MNRAS, 291, 658
Donati J.-F., Collier Cameron A., Petit P., 2003, MNRAS, 345, 1187
Donati J.-F. et al., 2006, MNRAS, 370, 629
Donati J. F. et al., 2020, MNRAS, 498, 5684
Donati J. F. et al., 2023a, MNRAS, 525, 455
Donati J. F. et al., 2023b, MNRAS, 525, 2015

Donati J. F. et al., 2024a, MNRAS, 530, 264
Donati J. F. et al., 2024b, MNRAS, 531, 3256
Donati J. F., Cristofari P. I., Carmona A., Grankin K., 2024c, MNRAS, 534, 231
Drążkowska J. et al., 2023, in Inutsuka S., Aikawa Y., Muto T., Tomida K., Tamura M.eds, ASP Conf. Ser. Vol. 534, Protostars and Planets VII. Astron. Soc. Pac., San Francisco, p. 717
Edwards S., Fischer W., Kwan J., Hillenbrand L., Dupree A. K., 2003, ApJ, 599, L41
Finociety B., Donati J. F., 2022, MNRAS, 516, 5887
Finociety B. et al., 2023, MNRAS, 526, 4627
Gaia Collaboration, 2023, A&A, 674, A1
Gaidos E., Thanathibodee T., Hoffman A., Ong J., Hinkle J., Shappee B. J., Banzatti A., 2024, ApJ, 966, 167
Gregorio-Hetem J., Hetem A., 2002, MNRAS, 336, 197
Gregorio-Hetem J., Lepine J. R. D., Quast G. R., Torres C. A. O., de La Reza R., 1992, AJ, 103, 549
Haffert S. Y., Bohn A. J., de Boer J., Snellen I. A. G., Brinchmann J., Girard J. H., Keller C. U., Bacon R., 2019, Nat. Astron., 3, 749
Hartmann L., Herczeg G., Calvet N., 2016, ARA&A, 54, 135
Hashimoto J. et al., 2012, ApJ, 758, L19
Haywood R. D. et al., 2014, MNRAS, 443, 2517
Hussain G., 2018, in Take a Closer Look. p. 26, doi:10.5281/zenodo.1488809
Isella A., Benisty M., Teague R., Bae J., Keppler M., Facchini S., Pérez L., 2019, ApJ, 879, L25
Jeffreys H., 1961, Theory of Probability, thirdedn. Oxford University Press, Oxford, England
Johns-Krull C. M., 2007, ApJ, 664, 975
Keppler M. et al., 2018, A&A, 617, A44
Keppler M. et al., 2019, A&A, 625, A118
Kochanek C. S. et al., 2017, PASP, 129, 104502
Kuffmeier M., 2024, Front. Astron. Space Sci., 11, 1403075
Kwan J., Edwards S., Fischer W., 2007, ApJ, 657, 897
Landi degl'Innocenti E., Landolfi M., 2004, Polarisation in Spectral Lines. Kluwer Academic Publishers, Dordrecht/Boston/London
Langlois M. et al., 2021, A&A, 651, A71
Lau T. C. H., Birnstiel T., Drążkowska J., Stammler S. M., 2024, A&A, 688, A22
Lehmann L. T., Donati J. F., 2022, MNRAS, 514, 2333
López-Valdivia R. et al., 2021, ApJ, 921, 53
Mann A. W. et al., 2022, AJ, 163, 156
Mordasini C., Alibert Y., Klahr H., Henning T., 2012, A&A, 547, A111
Pantolmos G., Zanni C., Bouvier J., 2020, A&A, 643, A129
Pecaut M. J., Mamajek E. E., 2013, ApJS, 208, 9
Press W. H., Teukolsky S. A., Vetterling W. T., Flannery B. P., 1992, Numerical Recipes in C. The Art of Scientific Computing, Cambridge University Press, Cambridge, USA
Pudritz R. E., Ray T. P., 2019, Front. Astron. Space Sci., 6, 54
Rajpaul V., Aigrain S., Osborne M. A., Reece S., Roberts S., 2015, MNRAS, 452, 2269
Romanova M. M., Ustyugova G. V., Koldoba A. V., Lovelace R. V. E., 2004, ApJ, 616, L151
Ryabchikova T., Piskunov N., Kurucz R. L., Stempels H. C., Heiter U., Pakhomov Y., Barklem P. S., 2015, Phys. Scr, 90, 054005
Sanderson H., Jardine M., Collier Cameron A., Morin J., Donati J. F., 2023, MNRAS, 518, 4734
Skilling J., Bryan R. K., 1984, MNRAS, 211, 111
Skinner S. L., Audard M., 2022, ApJ, 938, 134
Sousa A. P. et al., 2023, A&A, 670, A142
Thanathibodee T., Calvet N., Bae J., Muzerolle J., Hernández R. F., 2019, ApJ, 885, 94
Thanathibodee T. et al., 2020, ApJ, 892, 81
Thanathibodee T., Calvet N., Hernández J., Maucó K., Briceño C., 2022, AJ, 163, 74
Tsukamoto Y. et al., 2023, in Inutsuka S., Aikawa Y., Muto T., Tomida K., Tamura M.eds, ASP Conf. Ser. Vol. 534, Protostars and Planets VII. Astron. Soc. Pac., San Francisco, p. 317
Ustyugova G. V., Koldoba A. V., Romanova M. M., Lovelace R. V. E., 2006, ApJ, 646, 304
Xie C., Haffert S. Y., de Boer J., Kenworthy M. A., Brinchmann J., Girard J., Snellen I. A. G., Keller C. U., 2020, A&A, 644, A149
Zanni C., Ferreira J., 2013, A&A, 550, A99

APPENDIX A: ASAS-SN LIGHT CURVES AND STACKED PERIODOGRAMS

We show in Fig. A1, the ASAS-SN *V*-band (2014 May to 2018 September) and *g*-band (2017 December to 2024 August) light curves of PDS 70 (binned down to one point per night), along with the epochs of our SPIRou spectra and *TESS* observations. We also show in Fig. A2, the stacked periodograms of both light curves.

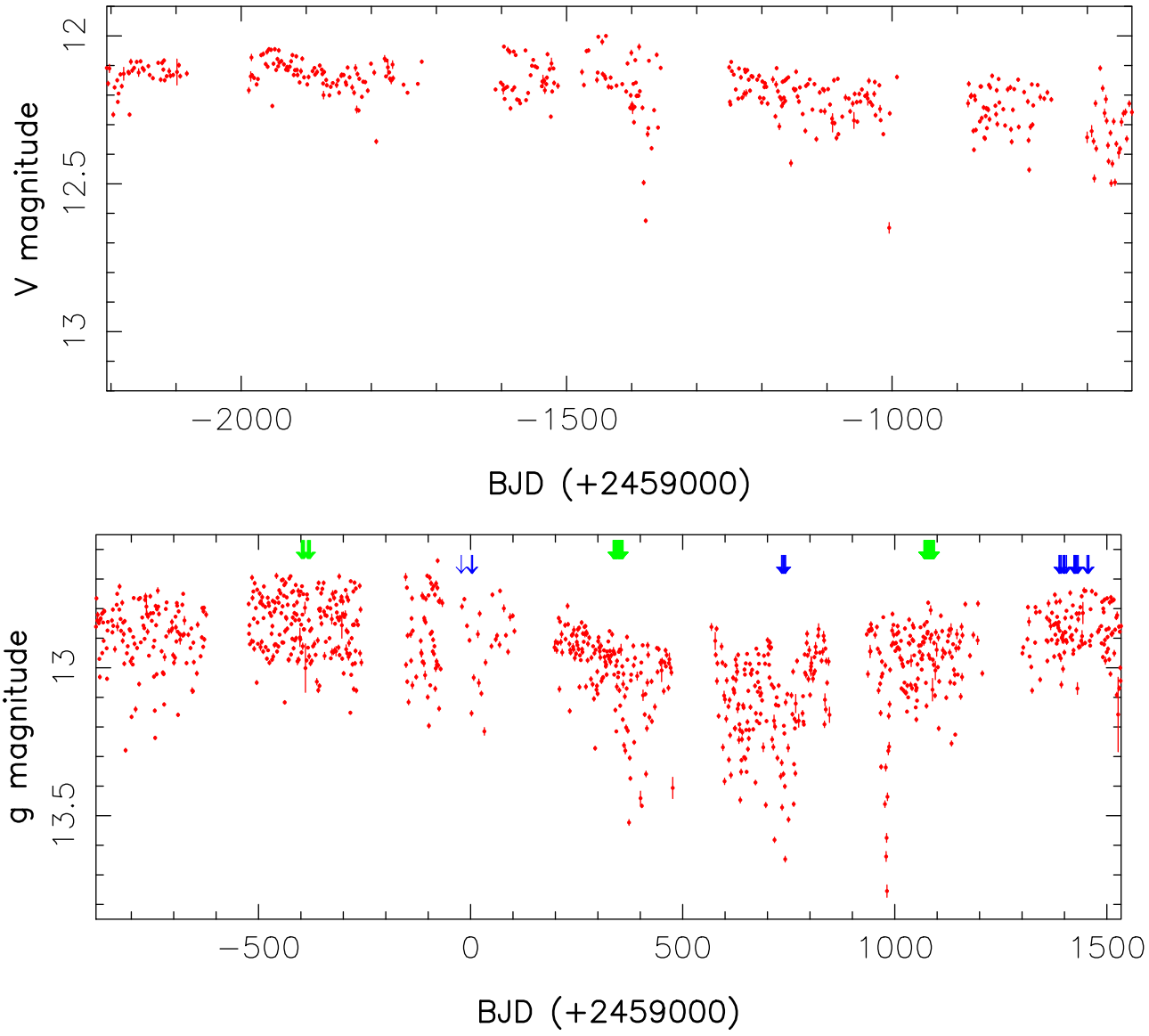

Figure A1. ASAS-SN *V*-band (2014 May to 2018 September, top panel) and *g*-band (2017 December to 2024 August, bottom panel) light curves of PDS 70, binned down to one point per night (red dots with error bars). On the second panel, we also depict the epochs of our SPIRou spectra (blue arrows) and of the *TESS* observations (sectors 11, 38, and 65, green arrows). Both panels have the same dynamic range to emphasize the temporal variations of the photometric fluctuations.

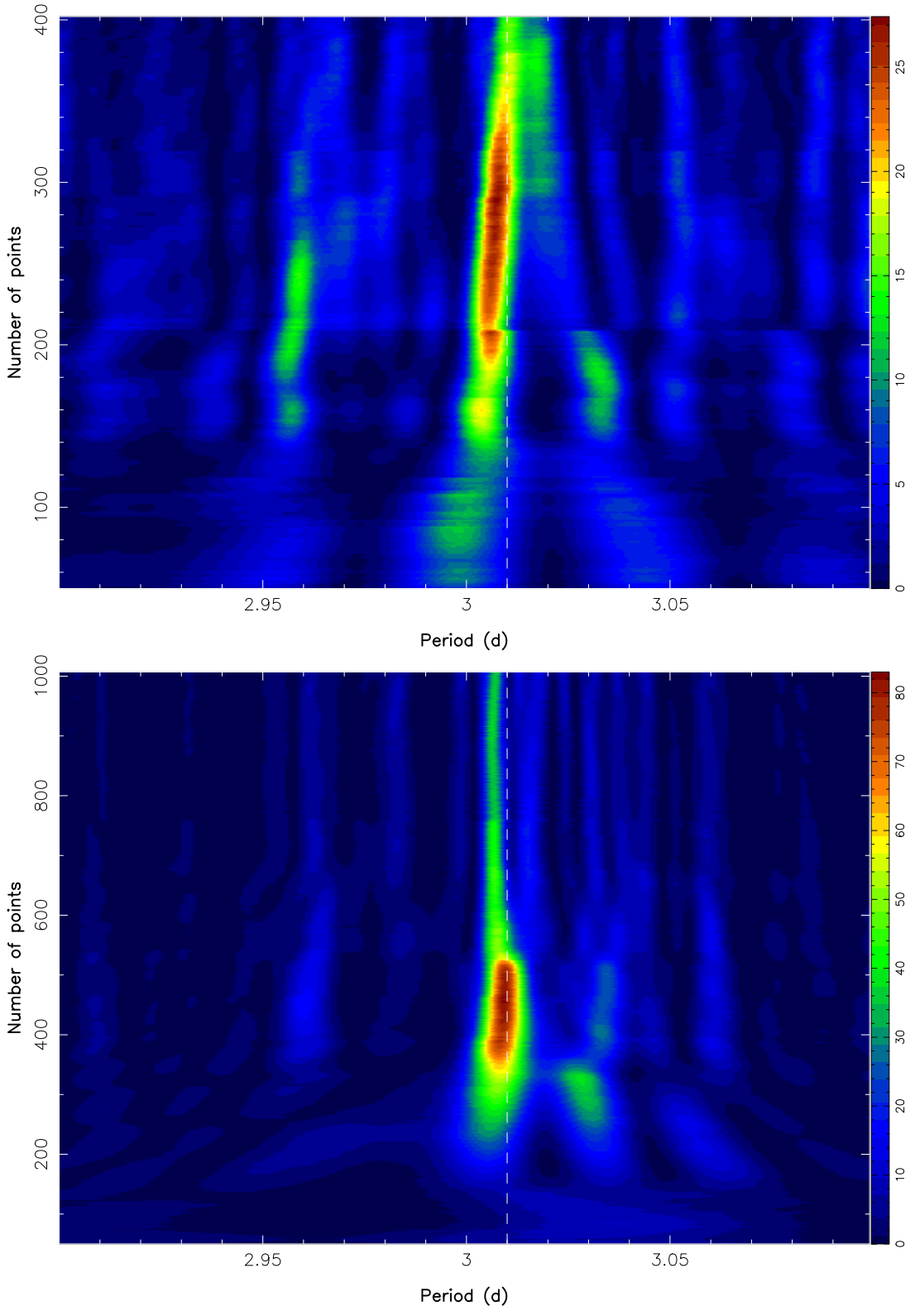

Figure A2. Stacked periodograms of the ASAS-SN V-band (top panel) and g-band (bottom panel) light curves of PDS 70 (see Fig. A1). In both plots, each horizontal line corresponds to a colour-coded periodogram, computed on an increasing number of points (starting from the first one). The colour scale (different in both panels) depicts the logarithmic power of each periodogram. A signal at a period of about 3 d is detected in both cases, its exact position and strength varying with time and weakening towards the end. The vertical dashed line depicts the rotation period as derived from our study.

APPENDIX B: OBSERVATION LOG

Table B1 gives the full log and associated B_ℓ, RV, BIS and FWHM measurements at each observing epoch from our SPIRou spectra.

Table B1. Observing log of our SPIRou observations of PDS 70 in seasons 2020, 2022, and 2024. All exposures consist of four subexposures of equal length, except on 2022 June 12, when bad weather only allowed for a pair of subexposures to be collected. For each visit, we list the barycentric Julian date BJD, the UT date, the rotation cycle c, and phase ϕ (computed as indicated in Section 3), the total observing time $t_{\rm exp}$, the peak SNR in the spectrum (in the H band) per 2.3 km s^{-1} pixel, the noise level in the LSD Stokes V profile, the estimated B_ℓ with error bars, the nightly averaged RVs, BISs, and FWHMs and corresponding error bars derived from Stokes I LSD profiles of atomic lines, the RVs and corresponding error bars of CO bandhead lines, and the veiling in the JH and in the K bands r_{JH} and r_K measured from LSD profiles of atomic and CO lines, respectively.

BJD (2459000 +)	UT date	c/ϕ	$t_{\rm exp}$ (s)	SNR (H)	σ_V ($10^{-4} I_c$)	B_ℓ (G)	RV (km s^{-1})	BIS (km s^{-1})	FWHM (km s^{-1})	RV (CO) (km s^{-1})	r_{JH}/r_K
−22.0907349	08 May 2020	0/0.003	2808.2	186	2.93	−37±19	5.79±0.17	1.93±0.21	32.3±0.5	6.06±0.55	0.18/0.56
1.8378984	01 June 2020	7/0.953	2808.2	183	3.50	−43±21	6.48±0.18	0.91±0.22	31.2±0.5	6.58±0.23	0.11/0.53
3.8672408	03 June 2020	8/0.627	2808.2	230	2.23	93±13	6.98±0.17	−0.70±0.22	31.3±0.5	6.51±0.24	0.08/0.46
4.8240857	04 June 2020	8/0.945	2808.2	224	2.25	−31±14	5.93±0.16	0.92±0.20	31.7±0.5	6.59±0.20	0.13/0.43
732.8321354	02 June 2022	250/0.808	2808.2	215	2.40	75±15	6.44±0.17	0.04±0.21	28.8±0.5	6.79±0.22	0.13/0.57
733.8368940	03 June 2022	251/0.142	2808.2	235	2.18	64±13	6.70±0.18	−0.95±0.22	30.5±0.5	6.89±0.22	0.10/0.58
735.8297289	05 June 2022	251/0.804	2808.2	241	2.10	55±12	6.26±0.16	0.19±0.20	29.0±0.5	6.64±0.18	0.10/0.72
736.8314022	06 June 2022	252/0.137	2808.2	233	2.17	55±13	6.62±0.17	−0.03±0.21	31.1±0.5	6.88±0.20	0.10/0.50
737.8318903	07 June 2022	252/0.469	2808.2	215	2.93	12±17	6.38±0.16	0.86±0.20	30.1±0.5	6.44±0.20	0.11/0.54
739.7949216	09 June 2022	253/0.121	2808.2	242	2.04	69±12	6.61±0.15	−0.58±0.19	31.4±0.5	7.08±0.26	0.10/0.35
740.8243867	10 June 2022	253/0.463	2808.2	230	2.14	29±12	5.89±0.15	1.12±0.19	30.8±0.5	6.24±0.19	0.05/0.44
741.8079906	11 June 2022	253/0.790	2808.2	224	2.21	74±13	5.64±0.15	0.93±0.19	29.5±0.5	6.02±0.19	0.13/0.98
742.7851079	12 June 2022	254/0.115	1404.1	110	4.63	86±30	6.93±0.17	−0.31±0.21	31.1±0.5	6.66±0.28	0.18/0.61
1387.0325927	17 Mar 2024	468/0.150	2808.2	206	2.30	176±13	6.81±0.16	−0.35±0.20	31.7±0.5	7.05±0.19	0.01/0.60
1388.0312781	18 Mar 2024	468/0.482	2808.2	215	2.22	71±13	6.00±0.16	−0.06±0.20	31.4±0.5	6.30±0.18	0.06/0.61
1389.0227861	19 Mar 2024	468/0.812	2808.2	238	1.95	−104±11	5.85±0.15	0.88±0.19	30.7±0.5	6.36±0.18	0.01/0.72
1391.0457659	21 Mar 2024	469/0.484	2808.2	187	2.61	86±15	6.11±0.16	0.88±0.20	32.0±0.5	6.62±0.25	0.09/0.32
1391.9946767	22 Mar 2024	469/0.799	2808.2	195	2.48	−103±14	5.75±0.16	1.08±0.20	30.7±0.5	6.57±0.26	0.04/0.31
1393.0092961	23 Mar 2024	470/0.136	2808.2	190	2.53	143±14	6.36±0.16	0.13±0.19	32.1±0.5	6.64±0.21	0.03/0.37
1397.0023396	27 Mar 2024	471/0.463	2808.2	223	2.12	64±13	6.33±0.18	0.13±0.22	31.5±0.5	6.81±0.22	0.10/1.02
1399.0130591	29 Mar 2024	472/0.131	2808.2	208	2.32	113±13	6.80±0.17	−0.21±0.21	32.3±0.5	7.37±0.20	0.03/0.46
1399.9973197	30 Mar 2024	472/0.458	2808.2	236	1.99	63±10	6.59±0.17	0.63±0.21	33.2±0.5	6.70±0.19	−0.06/0.31
1401.0273243	31 Mar 2024	472/0.800	2808.2	195	2.50	−116±13	5.78±0.16	1.31±0.20	30.8±0.5	6.49±0.20	−0.03/0.31
1401.9923358	01 Apr 2024	473/0.120	2808.2	232	1.99	128±10	6.86±0.18	0.01±0.22	32.7±0.5	7.09±0.20	−0.09/0.23
1405.0097796	04 Apr 2024	474/0.123	2808.2	165	3.15	135±18	7.28±0.17	−0.45±0.21	30.2±0.5	7.48±0.24	0.07/0.43
1421.9643985	21 Apr 2024	479/0.756	2808.2	216	2.24	−109±12	5.55±0.16	0.92±0.20	31.1±0.5	6.46±0.20	0.03/0.43
1422.9497230	22 Apr 2024	480/0.083	2808.2	241	2.00	91±11	6.72±0.16	−0.55±0.21	30.4±0.5	7.09±0.20	0.03/0.46
1423.9116919	23 Apr 2024	480/0.403	2808.2	230	2.10	124±11	6.56±0.16	−0.39±0.20	32.3±0.5	6.70±0.20	0.01/0.41
1424.8707088	24 Apr 2024	480/0.721	2808.2	245	1.90	−68±10	5.80±0.16	1.39±0.20	31.5±0.5	6.63±0.21	0.00/0.38
1425.9189887	25 Apr 2024	481/0.069	2808.2	206	2.37	78±13	6.33±0.16	−0.26±0.20	30.7±0.5	6.81±0.23	0.06/0.43
1426.9430337	26 Apr 2024	481/0.410	2808.2	217	2.19	113±12	6.79±0.16	−0.21±0.20	32.0±0.5	6.79±0.27	0.05/0.30
1427.8992940	27 Apr 2024	481/0.727	2808.2	243	1.97	−64±11	5.58±0.16	1.15±0.20	30.8±0.5	6.87±0.21	0.02/0.34
1429.9103948	29 Apr 2024	482/0.395	2808.2	120	4.77	172±29	6.04±0.18	0.16±0.22	31.1±0.5	6.87±0.31	0.14/0.51
1431.9180016	01 May 2024	483/0.062	2808.2	234	2.09	68±11	6.75±0.16	−0.24±0.20	31.2±0.5	7.29±0.36	−0.01/0.20
1432.9104947	02 May 2024	483/0.392	2808.2	227	2.17	145±12	6.53±0.17	−0.59±0.21	31.6±0.5	7.20±0.30	0.03/0.31
1452.9013731	22 May 2024	490/0.034	2808.2	232	2.17	39±12	6.81±0.17	−0.62±0.21	30.4±0.5	7.18±0.22	0.02/0.29
1454.8762118	24 May 2024	490/0.690	2808.2	187	2.73	−45±16	5.29±0.17	0.98±0.22	30.9±0.5	6.47±0.25	0.08/0.52
1455.8555552	25 May 2024	491/0.015	2808.2	183	3.47	60±19	6.50±0.17	−0.48±0.21	30.9±0.5	7.20±0.25	0.03/0.62
1456.8256793	26 May 2024	491/0.337	2808.2	133	4.26	94±26	7.08±0.18	−1.26±0.23	32.0±0.5	7.56±0.30	0.14/1.17
1457.8493597	27 May 2024	491/0.678	2808.2	241	2.06	−24±11	5.59±0.17	1.18±0.21	31.5±0.5	6.77±0.21	−0.02/0.34

APPENDIX C: RV PERIODOGRAMS

We show in Fig. C1, the periodograms of raw RVs, filtered RVs (i.e. raw RVs subtracted from the adjusted GP, see the text), and residual RVs (i.e. filtered RVs subtracted from the additional sinusoidal pattern, see the text) of PDS 70, resulting from the analysis described in Section 6.

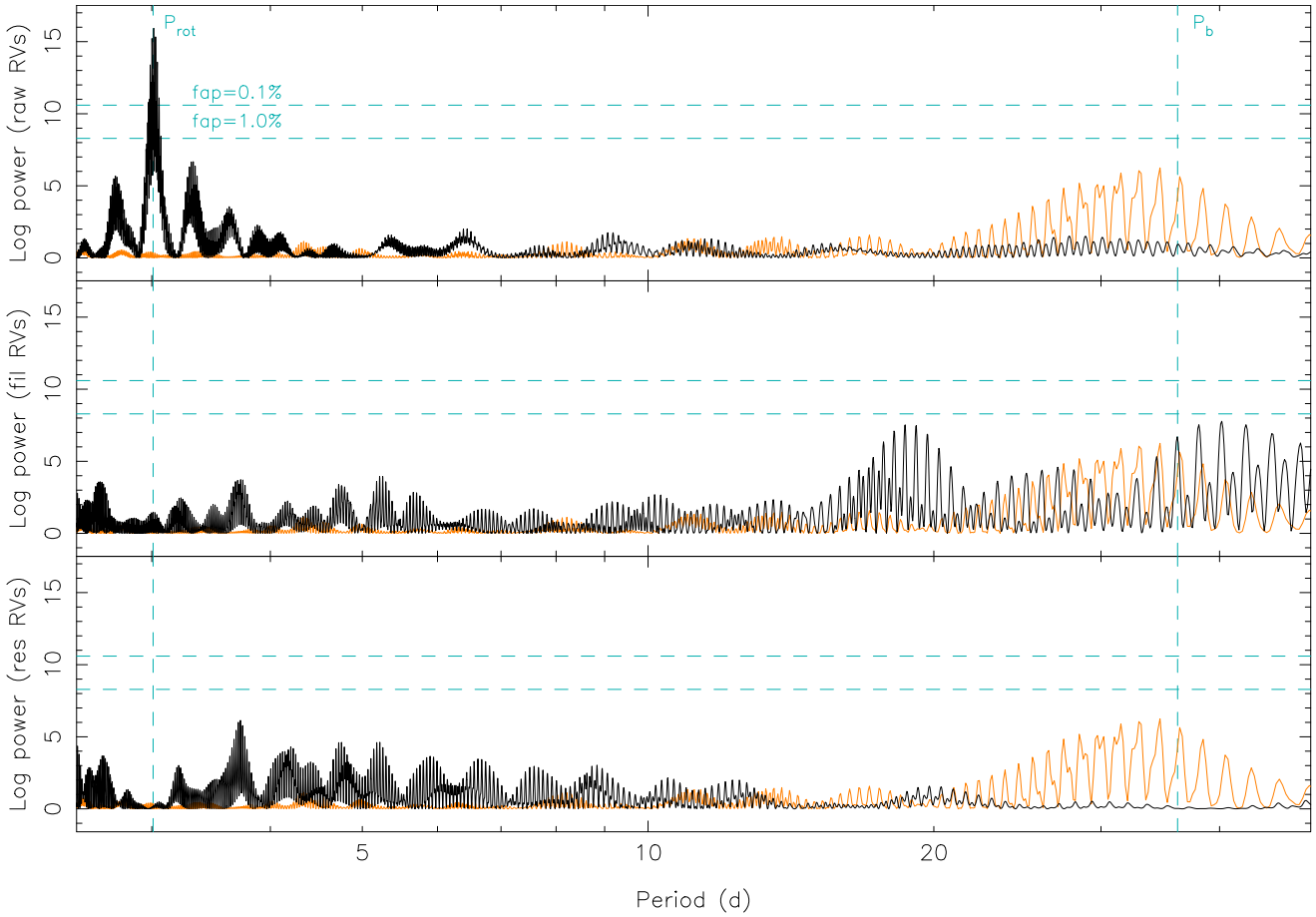

Figure C1. Periodograms of the raw RVs (top plot), filtered RVs (i.e. raw RVs subtracted from the adjusted GP, middle plot), and residual RVs (i.e. filtered RVs subtracted from the additional sinusoidal pattern, bottom plot) when including a sinusoidal fit at period of P_b in addition to the GPR modelling of the raw RVs in the MCMC process. The cyan vertical dashed lines trace the derived $P_{\rm rot}$ and P_b, whereas the horizontal dashed lines indicate the 1 per cent and 0.1 per cent FAP levels in the periodograms of our RV data. The orange curve depicts the periodogram of the window function. Excess power is visible in the periodogram of the filtered RVs around 20 and 40 d that is best modelled by a sinusoidal RV signal at $P_b = 36.16$ d (see Section 6).

This paper has been typeset from a TEX/LATEX file prepared by the author.